

**UNIVERSITY OF CALIFORNIA,  
IRVINE**

Engineered Protein Cage for Drug Delivery

**THESIS**

Submitted in satisfaction of the requirements  
for the degree of

**MASTER OF SCIENCE**

in Chemical and Biochemical Engineering

by

Mercè Dalmau Mallorquí

Thesis Committee:  
Professor Szu-Wen Wang, Chair  
Professor Nancy Da Silva  
Professor Andrew Putnam

2007



The thesis of Mercè Dalmau Mallorquí is approved:

---

---

---

Committee Chair

University of California, Irvine  
2007

To my parents and my sister

To Alfred

# Table of Contents

	Page
<b>List of Figures</b> .....	vii
<b>List of Tables</b> .....	ix
<b>Acknowledgements</b> .....	x
<b>Abstract of the Thesis</b> .....	xii
<b>Chapter 1 Introduction</b> .....	1
1.1 Protein nano-scaffolds .....	2
1.2 E2 subunit of pyruvate dehydrogenase .....	3
1.3 Objectives .....	6
<b>Chapter 2 Display of multifunctional peptides</b> .....	7
2.1 Introduction.....	7
2.2 Materials and Methods.....	10
2.2.1 Strains, vectors and media .....	10
2.2.2 Recombinant DNA techniques .....	11

2.2.3	Construction of expression vector .....	11
2.2.4	Expression and purification .....	14
2.2.5	Characterization with SDS polyacrylamide gel electrophoresis (PAGE). .....	15
2.2.6	Characterization with dynamic light scattering .....	16
2.3	Results and Discussion .....	16
2.3.1	Expression and purification .....	16
2.3.2	Characterization with dynamic light scattering .....	22
<b>Chapter 3 Studies on hydrophobic drug loading .....</b>		<b>24</b>
3.1	Introduction.....	24
3.2	Materials and Methods.....	29
3.2.1	Mutagenesis of internal cavity .....	29
3.2.2	Expression and Purification (1 L batch) .....	30
3.2.3	DCF standard curves and solubility limits determination.....	31
3.2.4	Determination of supersaturation required for nucleation .....	32
3.2.5	Preliminary study on dye-loading experiment.....	34
3.2.6	Sucrose gradient.....	35
3.3	Results and Discussion .....	36
3.3.1	Expression, purification and characterization of proteins.....	36
3.3.2	DCF standard curves and solubility limits determination.....	39
3.3.3	Determination of supersaturation conditions .....	43
3.3.4	Preliminary results on dye-loading experiment and sucrose gradient .....	46
<b>Chapter 4 Conclusions.....</b>		<b>50</b>

**Chapter 5 Future work**.....52

**References**.....54

# List of Figures

	Page
<b>Figure 1.1</b> Model for active-site coupling in a hypothetical E1E2E3 complex.....	4
<b>Figure 1.2</b> Electron micrographs of E2 wild-type.....	5
<b>Figure 2.1</b> 3-D view of the structure of the E2 core. ....	10
<b>Figure 2.2</b> Construction of expression vector pE2.....	12
<b>Figure 2.3</b> Example of new construct for expression of displaying RGD-4C peptide onto the E2 scaffold. ....	14
<b>Figure 2.4</b> 4-20% Tris-HCl SDS-PAGE of E2-RGD4C.....	17
<b>Figure 2.5</b> 4-20% Tris-HCl SDS-PAGE of E2-MAL1 at 37°C.....	17
<b>Figure 2.6</b> 4-20% Tris-HCl SDS-PAGE of E2-MAL1 at 30°C.....	18
<b>Figure 2.7</b> 4-20% Tris-HCl SDS-PAGE of E2-MAL1, LTV, RGD linear at 37°C.....	18
<b>Figure 2.8</b> 4-20% Tris-HCl SDS-PAGE of E2-J140 at 30 and 37°C.....	19
<b>Figure 2.9</b> Anion-exchange chromatography elution profile of E2-RGD4C.....	21
<b>Figure 2.10</b> 4-20% Tris-HCl SDS-PAGE of collected fraction after anion exchange chromatography.....	21
<b>Figure 2.11</b> Particle size analysis with DLS confirms overall particle size of the E2-RGD4C complex to be approximately 32.5 nm.....	23

<b>Figure 2.12</b> Particle size analysis with DLS confirms overall particle size of E2-WT complex to be approximately 28.7 nm.....	22
<b>Figure 3.1</b> Structure-view of one subunit of the E2 scaffold with residues Asp-381 (in green) and Lys-381 (in magenta).....	28
<b>Figure 3.2</b> 2',7'-dichlorofluorescein (Sigma) .....	28
<b>Figure 3.3</b> Schematic of the mutagenesis procedure.....	29
<b>Figure 3.4</b> Setup for sucrose gradient preparation .....	35
<b>Figure 3.5</b> Gel filtration chromatography elution profile of mutant D381F.....	37
<b>Figure 3.7</b> MALDI-TOF MS of mutant D381F.....	38
<b>Figure 3.8</b> Particle size analysis with DLS of the mutant D381F.....	39
<b>Figure 3.9</b> Absorbance spectrum of DCF in pure ethanol. ....	40
<b>Figure 3.10</b> Absorbance spectrum of 20 mM Tris buffer, pH 8.7. ....	40
<b>Figure 3.11</b> DCF standard curve in 20 mM Tris, pH 8.7.....	41
<b>Figure 3.12</b> DCF standard curve in 20 mM Tris and 8% ethanol, pH 8.7.....	41
<b>Figure 3.13</b> DCF solubility limits in Tris buffer at A) room temperature and B) 4°C.....	43
<b>Figure 3.14</b> Absorbance spectra of DCF solution (0.034 mg/mL) in 20 mM Tris and 8% ethanol pH 8.7.....	44
<b>Figure 3.15</b> Six replicates of supersaturation phenomenon at 8% ethanol and room temperature ([DCF]=3.3 mg/mL). ....	44
<b>Figure 3.16</b> Sucrose gradients.....	46
<b>Figure 3.17</b> Free DCF present in collected fractions. ....	48

# List of Tables

	Page
<b>Table 2.1</b> Primers DNA sequence .....	13
<b>Table 2.2</b> Summary of expression at 37°C and 30°C of different constructed plasmids.	20
<b>Table 3.1</b> Volumes of solutions used .....	36
<b>Table 3.2</b> Mean particle sizes of E2-WT and mutant M5 measured by DLS. ....	39
<b>Table 3.3</b> Coefficients of adjusted linear equations of standard curves at different ethanol percentages.....	42

# Acknowledgements

I want to dedicate some words of acknowledgement to those who were close to me and somehow made this work possible. First I would like to thank my advisor, Dr. Szu-Wen Wang, for giving me such opportunity, her guidance, brilliant advices and teaching me so much. I also would like to thank Mr. Pete Balsells and Dr. Roger Rangel, for providing me a way to come to the University of California, Irvine, through the Balsells Fellowship. Thanks to my committee members for their interest and devoted time, and to Prof. Ken Longmuir for the use of the dynamic light scattering instrument.

I also want to thank *my friends* from the Wang Lab Group for making me feel like just one more in the group and the wonderful times we have spent both inside and outside the lab. Special thanks to Sierin for teaching me all the molecular biology and protein purification skills I know, and her smiley face and personal support; and to Chengfei for the cultural exchange we did and becoming a great friend. Thanks to Polly and Matt for the interesting discussions on technical issues and making life more entertaining in the lab. I am also grateful to Cesar for his help and enthusiasm on this project.

Finalment, vull donar les gràcies als meus amics d'arreu per mantenir-me al dia malgrat la distància. En especial a la Judit per haver-me alegrat tantes nits amb les seves cròniques diàries.

Per acabar, l'agraïment més especial és pels meus pares Àngel i Agnès, sense els quals això no hauria estat possible. A ells els dec l'educació que m'han donat, la formació com a persona, i especialment l'estimació que han demostrat i tot el seu suport incondicional en tot moment. També vull agrair a la meva germana Anna els ànims i ajuda que sempre m'ha donat i sobretot, l'estima. I finalment, vull agrair molt especialment a l'Alfred tot el seu suport, paciència i estimació en tot aquest treball i el temps compartit.

# Abstract of the Thesis

## Engineered Protein Cage for Drug Delivery

By

Mercè Dalmau Mallorquí

Master of Science in Chemical and Biochemical Engineering

University of California, Irvine, 2007

Professor Szu-Wen Wang, Chair

The pyruvate dehydrogenase core protein (E2) from *Bacillus stearothermophilus* self-assembles into a 24-nm nanocapsule structure with a hollow inside core suitable for drug encapsulation and delivery. The external surface is hydrophilic, rendering it soluble in aqueous solution. In this work, we show the expression and characterization of different exogenous functional groups on the outside of the E2 scaffold, such as cell-targeting ligands for site-specific targeting, and quantum dot peptide for nucleation of inorganic nanoparticles that will enable reporting functionality. The internal cavity can be modified and the feasibility of hydrophobic loading with model drug molecules was

examined with promising results. Therefore, all these abilities make it a potential system for drug delivery.

# Chapter 1

## Introduction

One of the major problems that pharmaceutical companies are facing nowadays in drug discovery and development is the poor water solubility of new drugs [1, 2]. This issue translates to serious problems like lower bioavailability, and chemical and physical instability upon circulation inside the body. Many different strategies in drug delivery are being investigated to overcome these limitations. Drug delivery systems are designed to facilitate higher therapeutic efficiency delivery to desired targets while protecting the body from harmful side-effects through entrapment of drugs inside water-soluble scaffolds.

An ideal drug delivery system should be envisioned to tune release kinetics, to regulate biodistribution and to minimize toxic side effects, thereby decreasing drug doses and improving patient compliance. More specifically, the goals of drug delivery are (1) to surmount the limitations associated with biomacromolecular therapeutics, that is

insufficient stability, short plasma half-life and potential immunogenicity, and (2) to maximize the therapeutic potential while reducing the toxicity of side-effects [3, 4].

Advantages of using nanoparticles in the range of 10-100 nm for drug delivery and non-invasive imaging are (1) nanoparticles, due to their small size, penetrate even small capillaries and are taken up inside cells [5], reducing the risk of undesired elimination from the body through the liver or spleen [6] and minimizing their uptake by the reticuloendothelial system (RES) [7], (2) small particles have a higher surface area to volume ratios, thereby have greater dissolution rates, and (3) particles smaller than 50 nm can be internalized within endocytic vesicles (endosomes), penetrating inside the cell [8]. In conclusion, a target size range for drug delivery nanoparticles is 10 to 50 nm.

## **1.1 Protein nano-scaffolds**

Caged protein systems at the nanoscale, including viral capsids [9-15], heat-shock proteins [16, 17] and ferritin [18] have been proposed as general drug carriers for biomedical therapeutics and as imaging agents in medical diagnosis [17, 19, 20]. These biological systems have been investigated to assess their ability, when genetically manipulated, to incorporate onto the exterior surface of the cage exogenous biologically active molecules [12, 17]. Studies demonstrate the ability of these caged architectures to nucleate and attach metal nanoparticles both inside and outside [19, 21, 22].

Spherical protein cage assemblies are precisely self-assembled containers that occur naturally in different living organisms. These architectures consist of multiple copies of a specific number of protein subunits that self-assemble into these spherical

cages. It has been shown that these subunits are amenable to be modified by genetic and chemical techniques, without changing the overall assembly [23]. Therefore, they can incorporate simultaneously multiple functionalities within a single nanoparticle [14, 24]. Protein-based systems have a great potential as platforms for drug delivery with the advantage of a high degree of spatial organization with well-characterized self-assembly motifs that enable the control of functional group density and orientation [25]. Furthermore, it was shown that the effects of the immune system can be diminished by masking the recognition surface through pegylation [26] or by using humanized proteins.

To date, a few investigations have shown the ability of such scaffolds to covalently attach guest molecules (fluorescent molecules or drugs) inside the protein cage [16, 24, 27, 28]. But the ability of these protein systems for simultaneously targeting cells, *in vivo* imaging, and encapsulating and delivering drugs inside mammalian cells has not yet been reported.

## **1.2 E2 subunit of pyruvate dehydrogenase**

The pyruvate dehydrogenase (PDH) multienzyme complex is a key component in cellular metabolism. PDH is responsible for the conversion of pyruvate to acetyl-CoA and NADH, linking glycolysis to the citric acid cycle. PDH complexes with icosahedral symmetry are among the largest of cellular machines and are found in the mitochondria of eukaryotes and in Gram-positive bacteria such as *Bacillus stearothermophilus*. The detailed structure of PDH complexes from eukaryotes and bacteria have been elucidated using 3-D crystal diffraction [29]. The PDH complex consists of multiple copies of three

different enzymes: pyruvate decarboxylase (E1), dihydrolipoamide acetyltransferase (E2), and dihydrolipoamide dehydrogenase (E3) (Figure 1.1).

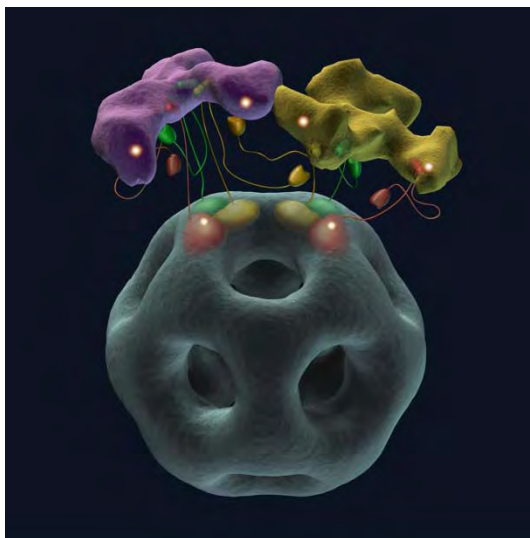


**Figure 1.1** Model for active-site coupling in a hypothetical E1E2E3 complex. Three E1 tetramers (purple) and three E3 dimers (yellow) are shown located in the outer protein shell above the inner icosahedron (gray) formed by 60 E2 catalytic domains. Figure reproduced from reference [28].

The E2 component of the *B. stearrowthermophilus* PDH complex is composed of a 28-kDa catalytic (acetyltransferase) domain, a 4-kDa peripheral subunit-binding domain (PSBD), and a 9-kDa lipoyl domain, which are connected by long stretches of polypeptide chain [27, 28]. In our research group, we have shown that the PSBD and lipoyl domains can be genetically removed to yield a core scaffold domain. The E2 component self-assembles into an icosahedron (Figure 1.2) that consists of 60 identical subunits forming a spherical shell with an outer diameter of 24 nm, 12 large openings of 5 nm diameter across the fivefold axes, and an inner core of 12 nm in diameter shown by crystallographic data [29].

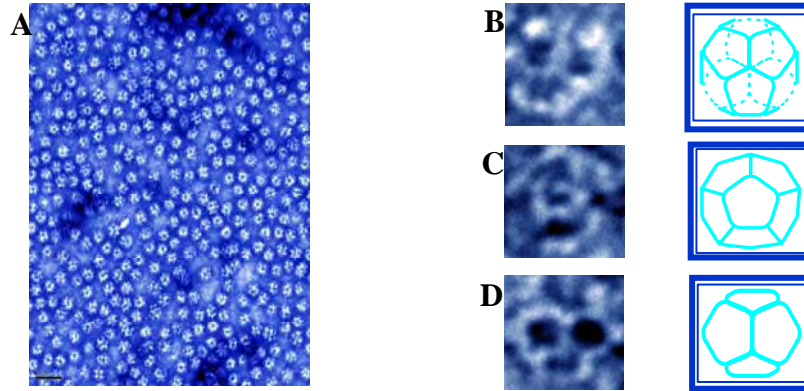


**Figure 1.2** Electron micrographs of core wild-type E2 negatively stained with uranyl acetate show correct assembly of 24-nm capsule. (A) A general view of a field of E2 molecules (scale bar 50nm). (B-D) Projections of E2 single molecules along the two, three, and five-fold axis.

Since the *B. stearothermophilus* PDH comes from a thermophilic organism, it has an intrinsic stability under extreme conditions [30]. In contrast with other self-assembled spherical structures, such as icosahedral virus capsids, the attachment of foreign peptides to the surface still enables the assembly of the E2 core [30]. This property is inherent to its natural configuration where the E2 core is fused to two independently-folding domains at its surface. Therefore, the E2 scaffold shows the potential to be used as a drug carrier for drug delivery purposes, as well as an imaging agent for therapeutic diagnosis.

## 1.3 Objectives

The overall goal of this thesis was to evaluate the E2 scaffold from *Bacillus stearothermophilus* as a drug delivery platform. First, the ability to obtain a correctly self-assembled E2 structure with exogenous peptides attached to the outer surface of the shell was analyzed. Therefore the following issues were studied:

- Construction and expression of recombinant genes coding for E2 with foreign peptides.
- Expression and purification of the recombinant proteins.
- Characterization of self-assembly through SDS-PAGE electrophoresis and dynamic light scattering (DLS).

Second, in order to determine the ability to nucleate a model drug inside the E2 cavity through hydrophobic interactions, the topics below were studied:

- Expression and purification of protein mutant with higher hydrophobicity in the inner core.
- Obtaining standard curves and solubility limits for model drug at different solvent concentrations.
- Determination of supersaturation conditions for model drug.
- Development of drug-loading protocol and separation through sucrose gradient.
- Evaluation of results through SDS-PAGE electrophoresis and absorbance measurements.

# **Chapter 2**

## **Display of multifunctional peptides**

### **2.1 Introduction**

The development of successful targeting agents will have major impacts for a number of medical applications, particularly improving the specificity of highly toxic drugs used to treat illnesses such as cancer or cardiovascular disease and in the diagnostic capabilities of imaging agents. To date, most drug delivery systems lack specificity for damaged tissue, and therefore may adversely affect surrounding tissue or suffer washout of the therapeutic component. Even though a variety of approaches have been developed to obtain cell-specific delivery of drugs, research on this area has not led to the development of a general therapeutically-viable targeted approach. The reason can be found to be the inability of the current delivery systems both to interact with the target cells and to overcome different barriers once inside the cell [3]. Therefore,

multifunctional vehicles with different capabilities to trigger the right site within the host are needed.

One of the most studied targeting peptides is the three amino acid sequence RGD (arginine-glycine-aspartate). This motif was found to be present in many adhesives proteins (such as fibronectin, collagens, fibrinogen and others) in the blood and extracellular matrices as their cell recognition site [31]. This sequence has been proved to bind both tumor cells and endothelial cells. Specifically, it binds selectively to integrins  $\alpha_v\beta_3$  and  $\alpha_v\beta_5$  which are up-regulated in angiogenic tumor vasculature [12, 22, 32-36]. *In vivo* studies demonstrated that the RGD-4C peptide can be utilized for cancer cell targeting either conjugated to a heat-shock protein or to the anticancer drug, doxorubicin [17, 37].

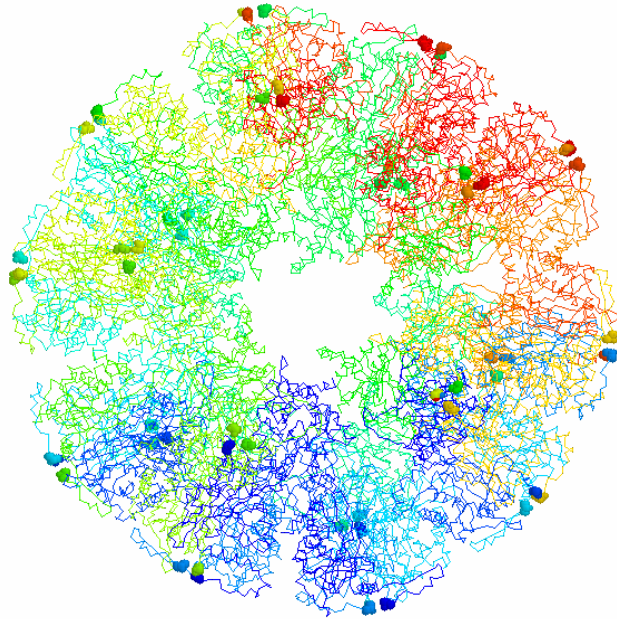
The display of peptides on the surface of a bacteriophage has been shown to be a productive tool to identify peptides for targeting organs, tumors, or cell type. Moreover, *in vivo* screening of peptide-phage libraries has made possible the identification of specific peptide ligands. An example of such peptides is the LTVSPWY peptide sequence which has been shown to internalize epithelial breast cancer cells [38].

Another functionality that can be conjugated to protein scaffolds is imaging capability. Non-invasive imaging has a great potential for the early detection and treatment of disease. Quantum dots (QDs) have received a great amount of attention for use as fluorescent labels in biological applications. QDs are small (<10 nm) inorganic nanocrystals that possess unique luminescent properties; their fluorescence emission is stable and tuned by varying the particle size or composition [39, 40]. Belcher and coworkers showed the viability of a virus-based scaffold to be used as a template for the

nucleation of different ZnS and CdS nanocrystal structures [41, 42]. Their potential has been shown for molecular imaging *in vitro* and *in vivo* [43].

Perham *et al.* were able to create chimeric E2 scaffolds displaying different peptides on the surface of the icosahedral E2 core. The E2 acetyltransferase core of *B. stearothermophilus* can be dissociated into unfolded monomers and refolded to the self-assembled caged core [44, 45]. They constructed multi-epitope chimeras displaying a histidine-tagged E2, a malaria epitope and a fluorescent protein (EGFP) [30]; and a vaccine displaying two different peptide epitopes of HIV-1 reverse transcriptase, which was able to induce an immune response in mice *in vivo* [46]. Thus, this demonstrates the flexibility of our scaffold for displaying at least two functionalities on its outer surface while keeping the self-assembly potential.

Our long-term goal is to evaluate the ability to obtain a correctly self-assembled E2 scaffold with multiple external peptides fused to the surface of the caged system (Figure 2.1). To date, no studies have reported more than two functionalities fused onto icosahedral protein structures. We expressed and characterized the stability of the new hybrid assemblies with external foreign ligands using dynamic light scattering (DLS). We were able to reproduce Domingo's work, and expressed the malaria epitope: MAL1 [30]. We constructed the vectors for three different cell-targeting peptides: cyclic RGD-4C, linear RGD and LTV, as well as one QD peptide for nucleating ZnS nanocrystals: J140. The RGD-4C was expressed in *E. coli* and its assembly characterized.



MDL

**Figure 2.1** 3-D view of the structure of the E2 core with the N-terminal of each monomer in spacefill view by using Protein Explorer<sup>®</sup> software. Peptide fusions to the N-terminus will result in peptides displayed on the surface of the scaffold.

## 2.2 Materials and Methods

### 2.2.1 Strains, vectors and media

*Escherichia coli* strain DH5 $\alpha$  (Zymo Research) was used for plasmid maintenance and construction, and *Escherichia coli* strain BL21(DE3) was used for protein expression. Plasmid pET11a (Novagen) that carries the T7 promoter-T7 terminator was used as a shuttle vector as well as an expression vector. Both *E. coli* strains were cultivated in Luria-Bertani (LB) medium [47] supplemented with 100  $\mu$ g/mL ampicillin.

### **2.2.2 Recombinant DNA techniques**

All *E. coli* DNA preparation was done with the QIAprep Spin Miniprep kit (Qiagen). DNA fragments were isolated from agarose gels by the QIAquick Gel Extraction kit (Qiagen). Polymerase chain reactions (PCR) were carried out under mineral oil in a reaction buffer (50  $\mu$ L) containing 20  $\mu$ M of each forward and reverse primer (Integrated DNA technologies), 0.1 U of *PfuUltra* Hotstart DNA Polymerase (Stratagene) on a programmable PTC-100 thermal cycler (MJ Research). The cycling parameters were as follows: 5 min at 95°C (one cycle); and 20 s at 95°C, 1 min at 68°C, and 1 min at 72°C (30 cycles) and 5 min at 72°C (one cycle). The amplified PCR fragments were purified using the QIAquick PCR Purification Kit (Qiagen), before sub-cloning into the vector. The fidelity of the amplified PCR fragments was confirmed by DNA sequencing after sub-cloning. DNA sequencing was performed at the UCI DNA Core, using the ABI PRISM<sup>®</sup> *BigDye3.1* (Applied Biosystems) protocol ([www.genome.uci.edu/DNAcore/download.htm](http://www.genome.uci.edu/DNAcore/download.htm)).

### **2.2.3 Construction of expression vector**

The expression of foreign polypeptides at the N-terminus of the catalytic acetyltransferase core domain of the *B. stearothermophilus* E2 was carried out using the plasmid pE2. This vector was constructed from the *E. coli* expression vector pET11a (Novagen) and the full length synthetic E2 gene that had been previously cloned into the CODABlue vector (CODA Genomics) by Dr. Sierin Lim (Figure 2.2). The synthetic E2

gene was engineered for high expression in *E. coli* by using computational methods (CODA Genomics; [48]).

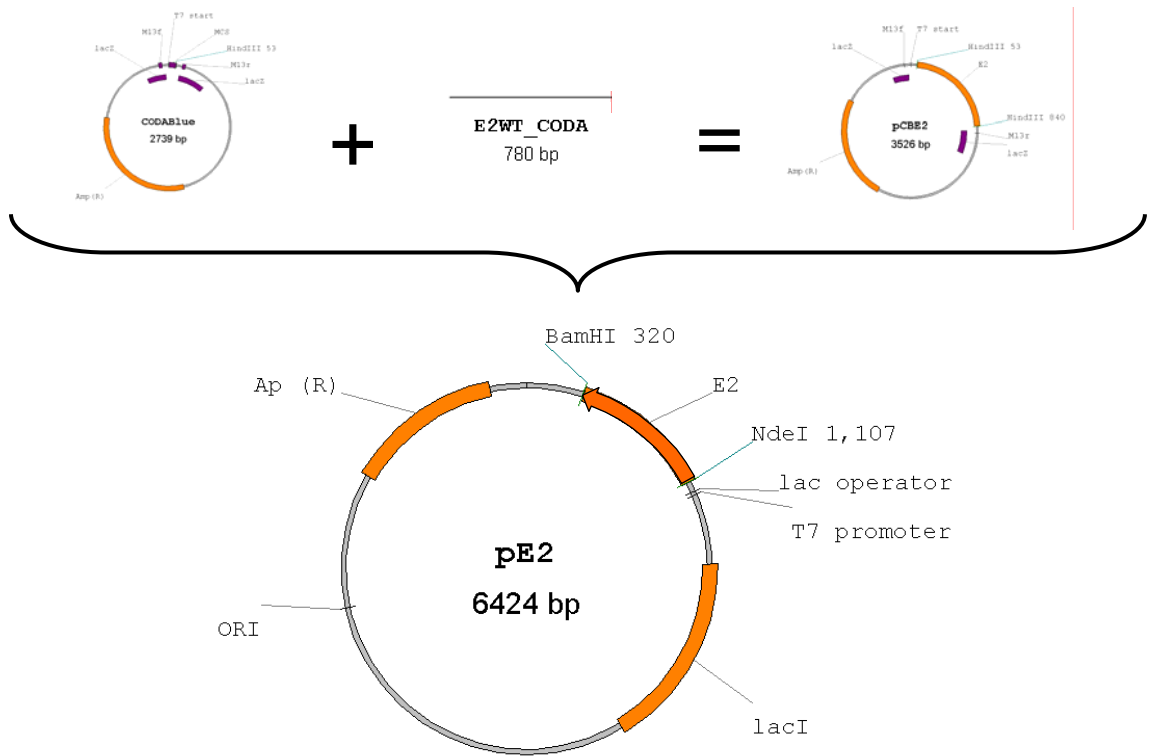


**Figure 2.2** Construction of expression vector pE2

All plasmids containing the gene for expression of the polypeptide chains at the N-terminus were constructed from the segment of DNA encoding the E2 core domain and a part of the linker sequence (residues Pro175-Ala 428 of the intact E2 chain) [30]. This DNA segment was PCR-amplified from pE2 using two oligonucleotides: forward primer, which encodes for the foreign peptides (see Table 2.1), and reverse, CGCGGATCCTTAAGCTTCCATCAGCAGCAG.

We decided to express one of the epitopes for malaria (MAL1) to reproduce Domingo's work [30], as a positive control. In order to compare two different peptides in

cell-targeting ability we chose the cyclic RGD-4C and the LTV since it has been shown to target carcinoma [22, 38]. Also, the linear RGD motif was constructed and expressed for comparison between the two different structural forms (cyclic and linear) in expression, self-assembly and targeting. And finally, for the imaging functionality, a peptide (J140) encoding a sequence which nucleates ZnS quantum dots was chosen [42].

Name	Peptide sequence (aa)	Primers
MAL1	NANPNANPNANP	G GAA TTC CAT ATG GGC AAT GCA AAC CCG AAC GCA AAC CCG AAT GCA AAC CCG CCT GGT CC
RGD-4C	CDCRGDCFC	G GAA TTC CAT ATG GGC TGC GAT TGC CGT GGC GAT TGC TTT TGC CTG TCT GTT CCT GGT CC
LTV	LTVSPWY	G GAA TTC CAT ATG GGC CTG ACC GTG AGC CCG TGG TAT CTG TCT GTT CCT GGT CC
RGD(linear)	GRGDSLSV	G GAA TTC CAT ATG GGC CGT GGC GAT AGC CTG TCT GTT CCT GGT CC
J140	SLTPLTTSHLRSGASGA	G GGA TTC CAT ATG GGC AGC CTG ACC CCG CTG ACC ACC AGC CAT CTG CGT AGC GGC GCA AGC GGC GCA CCT GGT CC

**Table 2.1** Primers DNA sequence

The amplified PCR product and the vector pET11a were digested with the restriction enzymes *NdeI* and *BamHI* (New England Biolabs). Both DNA fragments were gel extracted and ligated with phage T4 DNA ligase (New England Biolabs). The new plasmid was transformed into *E. coli* DH5 $\alpha$ , and colonies hosting the desired plasmid DNA were selected on LB medium plates containing ampicillin. Plasmid DNA were prepared and successful construction of the plasmid (Figure 2.3) was confirmed by DNA sequencing.

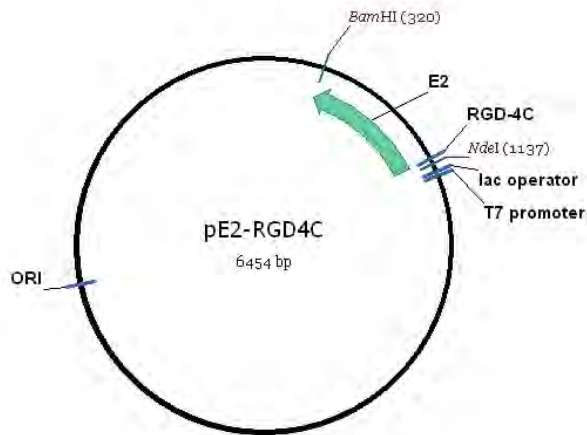


**Figure 2.3** Example of new construct for expression of displaying RGD-4C peptide onto the E2 scaffold.

## 2.2.4 Expression and purification

*E. coli* BL21(DE3) cell colonies were transformed with the new constructed plasmids by using a standard heat shock method [47], and selected on LB medium plates containing ampicillin. For each construct, 3 colonies were screened for expression at 30 and 37°C in LB medium supplemented with 100 µg/mL ampicillin. For each colony, 100 µL from an overnight culture of cells was used to inoculate 5 mL of medium. When the OD<sub>600</sub> was between 0.6 and 0.8, the inducer isopropyl-1-thio-β-D-thiogalactoside (IPTG) was added to a final concentration of 1 mM. The cells were harvested 3 h after induction by centrifugation (Beckman Coulter) at 2345 g for 15 min. *E. coli* cells were resuspended (in 1/10 volume of culture) in 20 mM Tris/HCl, 10 mM EDTA, 0.02% sodium azide, 0.1 mg/mL RNase and 0.1 mg/mL DNase (pH 8.7) on ice. The suspension was then disrupted by 3 cycles of sonication (Fisher Scientific). Cell debris was removed by centrifugation at 17500 g for 15 min. Expression was characterized on a SDS polyacrylamide gel.

For clones that expressed the recombinant protein in the soluble fraction, the expression was scaled-up to a culture volume of 100 mL for protein purification. The disruption process and recovery of the soluble protein was the same as for the 5 mL culture. Then, the supernatant was heat treated at 75°C for 20 min to precipitate *E. coli* proteins and centrifuged at 274000 g for 1 h. The soluble fraction was applied at a flow rate of 1 mL/min onto a 1 mL HiTrap Q-Sepharose FastFlow (FF) anion-exchange column (GE Healthcare), equilibrated with 20 mM Tris/HCl, 1 mM EDTA and 0.02% sodium azide pH 8.7 (Buffer A). The recombinant protein was eluted with a linear gradient of 0-1 M NaCl in Buffer A at a flow rate of 1 mL/min. One-mL fractions containing the recombinant protein were pooled and run (at a flow rate of 0.5 mL/min) onto a Superose 6 10/300 GL gel filtration column (GE Healthcare) previously equilibrated with 20 mM Tris/HCl, 150 mM NaCl, 0.02% sodium azide and 1 mM EDTA (pH 8.7).

### **2.2.5 Characterization of purified protein with SDS polyacrylamide gel electrophoresis (PAGE)**

A 20 µL sample was mixed with the same volume of loading buffer solution (1.25 mL of 0.5 M Tris/HCl pH 6.8; 1.0 mL of 10% (w/v) SDS; 2.5 mL of glycerol; 0.2 mL of 0.5% bromophenol blue; 0.5 mL of 2-mercaptoethanol and 3.55 mL of ultrapure water) and heated to 95°C for 5 minutes. The denatured sample (12.5 µL) was then loaded onto a 4-20% Ready Gel Tris-HCl (BioRad). Five-µL of the Perfect Protein Marker 10-225 kDa (Novagen) was used to indicate protein size on the gel. A constant

200 V was applied to the gel in the Mini-Protean3 system (BioRad) and electrophoresis was completed in 45 minutes. The gels were then stained for protein using Imperial Protein Stain (Coomassie dye-based reagent, Pierce) following the manufacturer's protocol. Digital pictures were taken with the AlphaImager (Alpha Innotech) and its software.

### **2.2.6 Characterization with dynamic light scattering**

Dynamic light scattering (DLS, Zetasizer Nano-ZS, Malvern) measurements of recombinant protein in aqueous solution were performed to determine the hydrodynamic radii of the nanocapsules and confirm the formation of the correctly-assembled core of the recombinant protein nanocapsules.

To prepare DLS samples, the purified protein solution (~1 mg/mL) was mixed and filtered using a 0.22  $\mu\text{m}$  syringe filter. DLS was measured at 25°C using a 4mW He-Ne, 633 nm laser, and the correlation functions were fit using a non-negatively constrained least squares (NNLS) fitting algorithm.

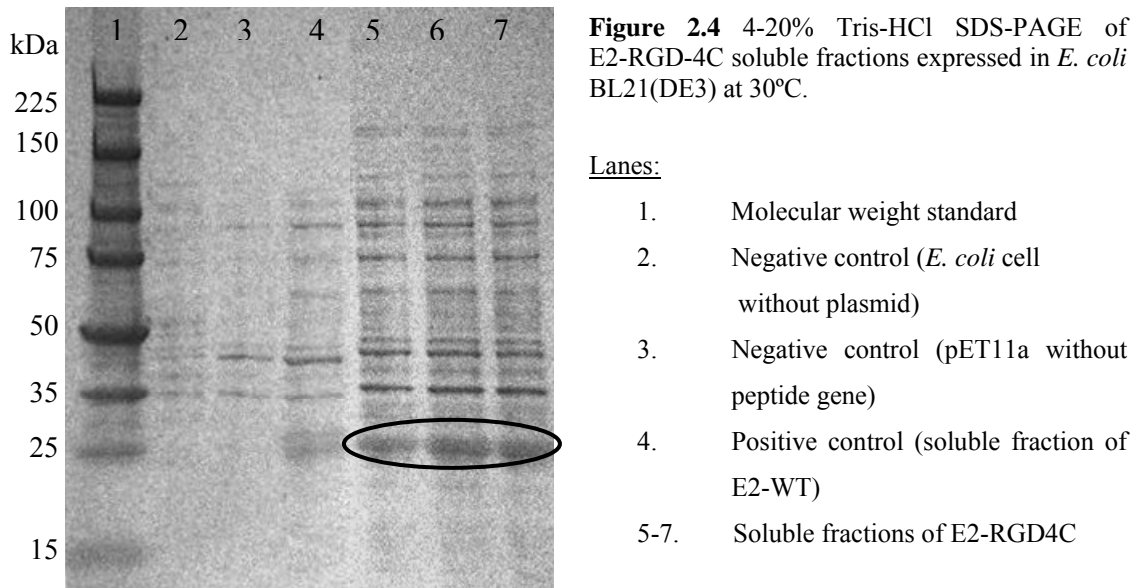
## **2.3 Results and Discussion**

### **2.3.1 Expression and purification**

All five vector constructs detailed in Table 2.1 were obtained and their correct DNA sequence confirmed. These plasmids were transformed into *E. coli* BL21(DE3) and checked for expression at 30 and 37°C. To detect the formation of the recombinant

proteins, standard SDS-PAGE gels were used to visualize the expressed protein in the cell extract. A summary of the results is shown in Table 2.2.

Figure 2.4 shows soluble fractions of three different clones expressing the peptide RGD-4C at 30°C. This peptide could be expressed at both 30 and 37°C, but the highest expression yield in the soluble fraction was obtained at 30°C.



The MAL1 peptide was also expressed in the soluble fraction at both temperatures (30 and 37°C) (Figure 2.5 and 2.6), but the highest expression was obtained at 30°C (Figure 2.6).

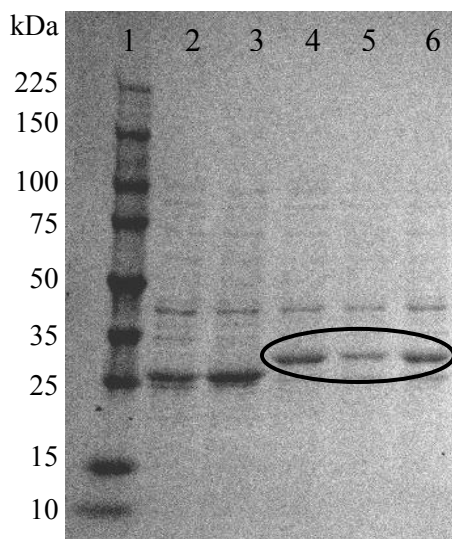


**Figure 2.5** 4-20% Tris-HCl SDS-PAGE of E2-MAL1 soluble fractions expressed in *E. coli* BL21(DE3) at 37°C.

Lanes:

1. Molecular weight standard
- 2-3. Positive control (soluble fractions of E2-WT)
- 4-6. Soluble fractions of E2-MAL1

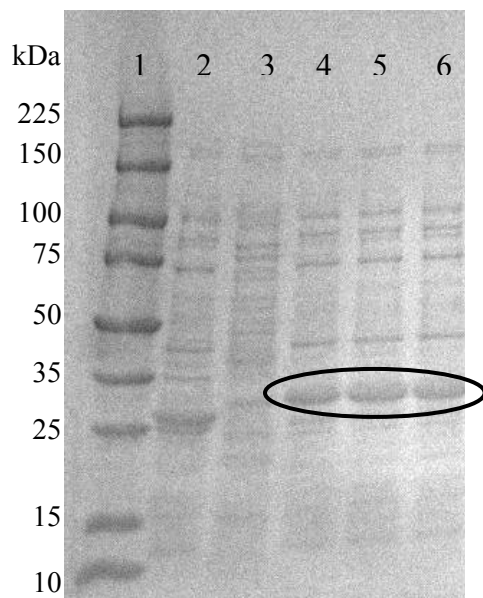
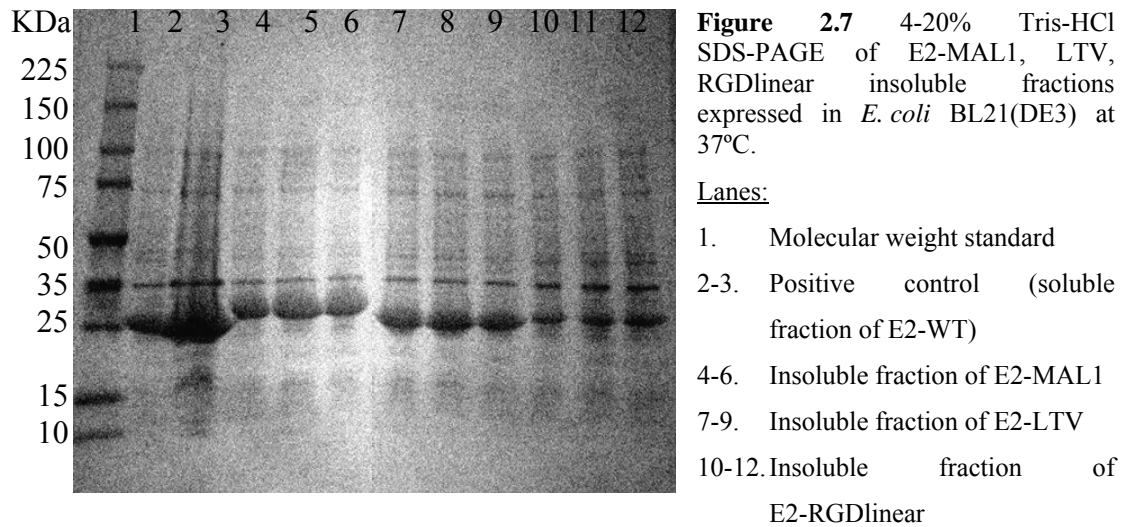


**Figure 2.6** 4-20% Tris-HCl SDS-PAGE of E2-MAL1 soluble fractions expressed in *E. coli* BL21(DE3) at 30°C.

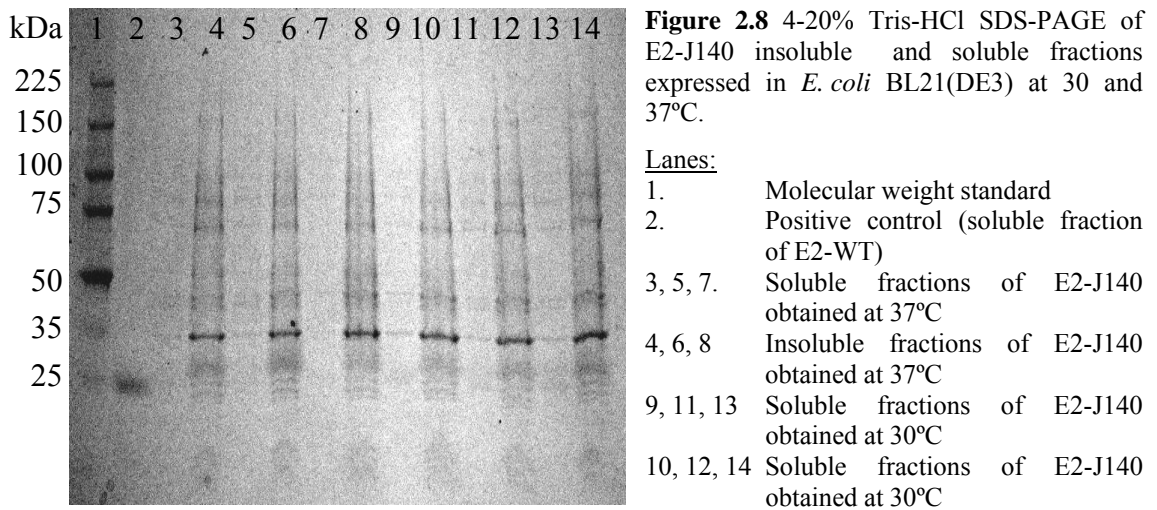
Lanes:

1. Molecular weight standard
2. Positive control (soluble fraction of E2-WT)
3. Negative control (pET11a without peptide gene)
- 4-6. Soluble fractions of E2-MAL1

The other two cell-targeting peptides, LTV and RGDlinear, were expressed in the insoluble fraction at 37°C (Figure 2.7) and in a very small amount in the soluble fraction at both temperatures, compared to the MAL1 and RGD-4C.



Expression of QD peptide (J140) was tested at 30 and 37 °C, but results from SDS-PAGE were inconclusive since not enough sample was loaded for detection in the soluble fractions (Figure 2.8). Its expression yield relative to MAL1 was very low.



In summary, both peptides MAL1 and RGD-4C were expressed in the soluble fractions with high levels at 30°C. Both LTV and RGDlinear could be expressed at a lower rate

compared to the previous two at both temperatures, and the quantum dot peptide was detected in the insoluble fraction for both tested temperatures, and expression in the soluble fraction was not clear. This variability in expression suggests that mutations at the N-terminus of the expressing gene are critical for proper folding and expression of the recombinant protein (Table 2.2).

Peptide	Amino acid sequence	Expression at 37°C		Expression at 30°C	
		Insoluble	Soluble	Insoluble	Soluble
MAL1	NANPNANPNANP	+++	++	+	+++
RGD-4C	CDCRGDCFC	+++	+	+++	++
LTV	LTVSPWY	+++	+	+++	+
RGDlinear	GRGDSLSV	++	+	++	+
J140	SLTPLTTSHLRSGASGA	+	?	+	?

**Table 2.2** Summary of expression at 37°C and 30°C of different constructed plasmids.

After checking the expression of the E2-RGD4C protein, the soluble fraction was purified using a HiPrep Q FF column in the Fast Protein Liquid Chromatography (FPLC). The collected fractions were loaded on a SDS-PAGE gel to identify the recombinant protein. A single clear band at the target protein size was found in fraction number A11 (Figure 2.9 and Figure 2.10), although impurities of larger size are still present after the Q FF purification step as can be seen in Figure 2.10. Therefore, another step of purification should be performed to further eliminate the larger size impurities. Our subsequent purification protocols include an additional size exclusion purification step (see Chapter 3).

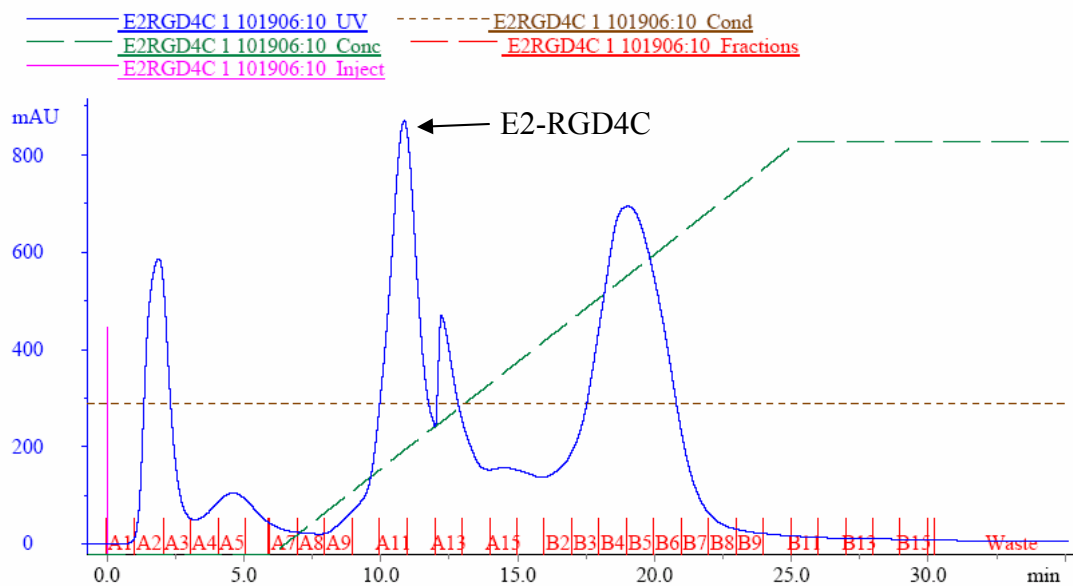


**Figure 2.9** Anion-exchange chromatography elution profile of E2-RGD4C.

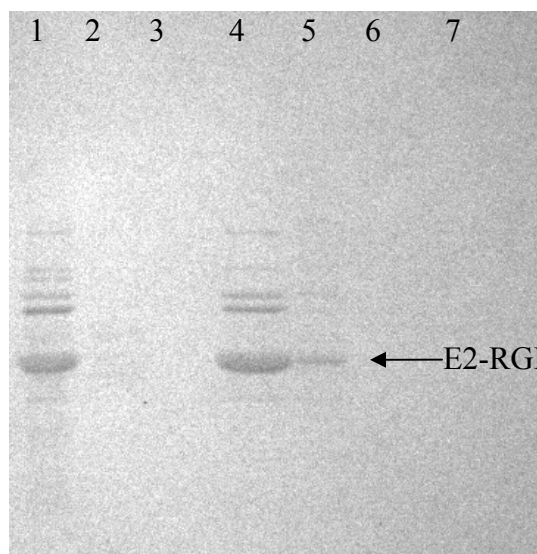


**Figure 2.10** 4-20% Tris-HCl SDS PAGE of collected fractions after anion exchange chromatography.

Lanes:

1. Soluble fraction loaded into the HiPrep Q FF column.
2. Collected fraction A2
3. Collected fraction A5
4. Collected fraction A11
5. Collected fraction A13
6. Collected fraction B4
7. Collected fraction B5

In order to improve the overall yield of protein recovery, several actions can be performed. Cell lysis is one step that could be optimized. Our experimental results have shown that the French<sup>®</sup> press has a higher efficiency in protein recovery than sonication. The French<sup>®</sup> press homogenizer uses high pressure to disrupt cell membranes while the sonicator uses high frequency waves to shear cells. Another stage to be optimized is the

purification step. This could be done by injecting the largest volume allowed according to the column size and the filling resin used in order to be able to separate the desired protein from impurities. This way, a concentration step after the Q FF column may not be required (step at which some protein is lost due to its deposition onto the membrane).

### 2.3.2 Characterization with dynamic light scattering

After purification, the formation of correctly assembled E2 nanocapsule displaying RGD-4C peptide onto its outer surface was confirmed by dynamic light scattering (DLS) and compared to the E2-WT. The measured particle size was close to the theoretical calculated 31.5 nm of the E2 scaffold expressing the cyclic peptide (Figure 2.11) and slightly higher than the measured size of the E2-WT (Figure 2.12) due to the display of 60 peptides on the outer surface.

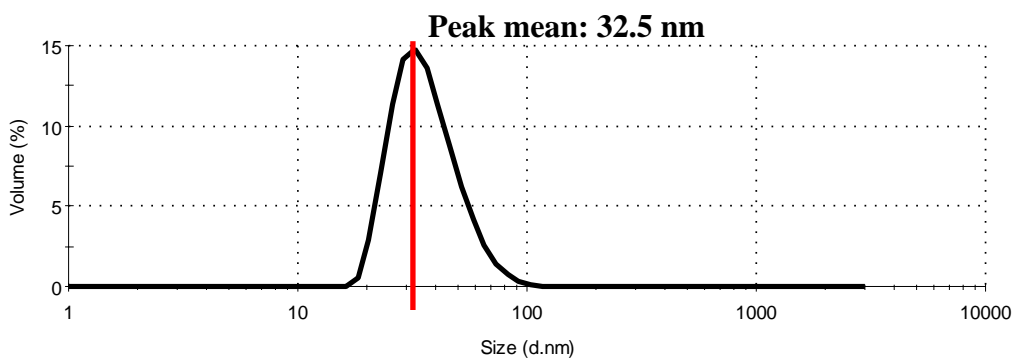


**Figure 2.11** Particle size analysis with DLS confirms overall particle size of the E2-RGD4C complex to be approximately 32.5 nm.

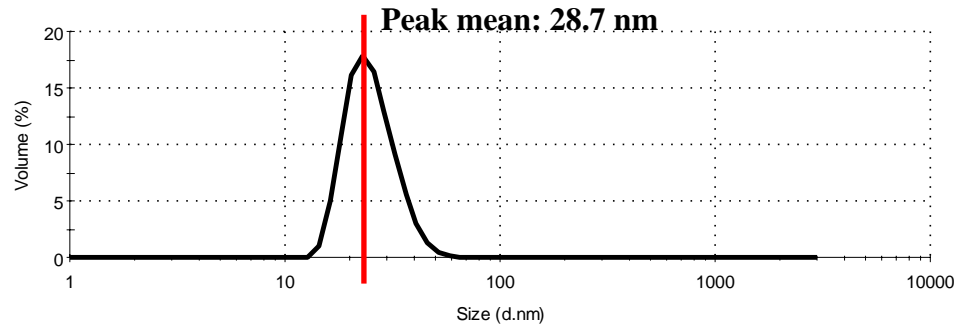


**Figure 2.12** Particle size analysis with DLS confirms overall particle size of E2-WT (control) to be approximately 28.7 nm.

Note that the hydrodynamic values are expected to be generally larger than the actual diameters because of counterion cloud contributions to particle mobility [49].

Using TEM as a confirmation of structure (Figure 1.2), we have shown (in previous work in our lab) that DLS values between ~23-35 nm have corresponded to correctly-assembled nanocapsules. Our results therefore indicate that we can fuse functional peptides onto the surface of our scaffold and still yield the correct icosahedral assembly.

# Chapter 3

## Studies on hydrophobic drug loading

### 3.1 Introduction

The interior cavities of self-assembled nanocaged structures are hollow and thus are potentially suitable to serve as platforms for encapsulation and release of guest molecules. Current approaches include chemical and genetic manipulation. One of the most used methods is the covalent attachment to site-specifically engineered residues on the interior surface. Thus, a cysteine residue genetically introduced at the inner surface presents a reactive thiol group in the assembled protein cage. Flenniken *et al.* covalently modified Hsp cage interior and selectively attached fluorescein molecules to the reactive cysteines with a pH-sensitive linker [16, 17]. The utility of this approach has been demonstrated with the attachment and release of the anticancer drug doxorubicin using a virus-like cage [24] and imaging agents [50]. Schmidt *et al.* inserted the WW domain (a small and compact globular structure that is characterized by two highly conserved

tryptophan residues and interacts with proline-rich ligands) of mouse Formin binding protein 11 (FBP 11) to the N-terminus of VP1 (which faces the interior of the capsid), and attached proline-rich ligands to the inner surface of the virus-like particles [51]. These virus-like encapsidated scaffolds were able to penetrate mammalian cells and deliver peptides and proteins *in vitro*.

Another approach for molecular entrapment using virus-like scaffolds is a pH-dependent gating mechanism used by Douglas *et al.* [52]. Many viruses can experience reversible structural changes that open or close the pores on the scaffold. Under swollen conditions, free molecular exchange between the virus cavity and the medium allows the entrapment of materials. They showed the ability to couple this swelling mechanism of the cage with a pH-dependent inorganic polymerization for the entrapment and crystallization of two mineral particles. Also, they demonstrated the electrostatic interactions between the scaffold and the guest molecules by a pH-dependent encapsulation of an anionic organic polymer. Thus, this approach was shown to be versatile for guest molecules encapsulation.

Other protein-based systems used in drug encapsulation include human serum albumin (HSA) and protein-based polymers. Microcapsules of HSA can be produced by the stabilization of an emulsified solution of albumin in the presence of drug, by heating or addition of a cross-linking agent [53-55]. Thus, drug solubility and stability can increase and alter pharmacokinetic profiles [53, 56]. However, the use of HSA as a pharmaceutical excipient is still very empirical. One of the most exploited protein-based polymers are the elastin-like polymers (ELP) [57]. Nanoparticles of ELP can be loaded with significant amounts of a model drug dexamethasone phosphate (DMP) when

self-assembling is carried out in an aqueous co-solution of polymer-DMP by raising the temperature from 4°C to 37°C. This temperature change induces the polymer to fold into a non-random structure called a  $\beta$ -spiral. In this folded state the polymer chain loses all the water structures from hydrophobic hydration and this water is mostly placed inside the hydrophilic channel within the  $\beta$ -spiral, where the DMP is entrapped [57, 58].

The development of high-throughput screening technology in drug discovery allows the massive emergence of new drug candidates. Nevertheless, it has been reported that poor aqueous solubility is the predominant problem associated with high-throughput tested drug candidates [1].

Thus, our objective was to design a generalized protein scaffold to encapsulate and solubilize a broad range of drug molecules while decreasing toxicity of side-effects, maintaining drug stability, and retaining therapeutic activity. Therefore, we first had to analyze generalized drug-protein interactions. These types of interactions have been studied in multi-drug efflux transporters. Efflux pumps are known to be present in most living cells. In human cells, pumps such as P-glycoprotein (P-gp) were found to prevent the entry of toxic molecules and to decrease cellular accumulation of drugs. Since P-gp has broad substrate specificity, with over 100 different known substrates [59], the key point was to elucidate the nature of this substrate recognition. Further studies reported that the nature of this chemical specificity is mostly hydrophobic with some electrostatic interactions (aromatic stacking and Van der Waals forces) [60-62]. Therefore we hypothesize that the protein nanocapsule design must incorporate a significant amount of accessible hydrophobic residues in the internal cavity wall.

The introduction of hydrophobic residues on the interior cavity of the E2 cage was performed via mutagenesis of the E2 wild type. The requirements of the sites to be mutated were: (1) be within the internal cavity, (2) not be involved in any interactions with adjacent subunits, and (3) be charged amino acids to maximize the increase of hydrophobicity relative to the E2 wild type. Since the protein nanocage is an assembly of 60 identical subunits, a single mutation and double mutation result in 60 and 120 mutations in a single nanocapsule, respectively.

Protein Explorer<sup>®</sup> software and the crystallographic structure of the E2 subunit from the Protein Data Bank were used to find possible mutation sites. Two sites were identified within the E2 complex: Asp-381 (in a loop region) and Lys-239 (in an alpha-helix) (Figure 3.1). These two residues were mutated to a phenylalanine (Phe) since in nature P-gp uses Phe residues for binding diverse hydrophobic drug molecules [63, 64]. Previous studies in our lab had shown the potential of the mutant D381F for drug encapsulation among the different mutants obtained. Both K239F, D381F, and wild-type proteins were expressed and tested for encapsulation of 2', 7'-dichlorofluorescein (DCF) by nucleation of this dye inside the scaffolds. Only the D381 sample showed DCF coeluting in the same fraction as the protein when separated onto a sucrose gradient. Due to the nature of the experiment, the conditions could not be duplicated, and repeatability of this result was variable. Therefore, we decided to systematically investigate the steps of this approach with the D381F mutant.

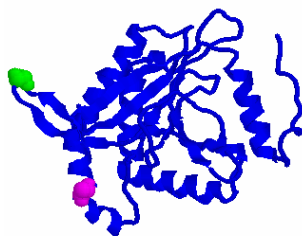


**Figure 3.1** Structure-view of one subunit of the E2 scaffold with residues Asp-381 (in green) and Lys-381 (in magenta) by using Protein Explorer<sup>®</sup> software.

Our overall goal was to develop a general assay to entrap a broad range of hydrophobic drug molecules inside the E2 nanocage. Thus, a hydrophobic model drug (2',7'-dichlorofluorescein, DCF) (Figure 3.2) was used for these preliminary studies. To date, most of the procedures employed to position the drug inside the cavity of protein scaffolds have been chemical-reaction-based; therefore, the physicochemical properties and therapeutic activity of drugs can be easily affected. For these reasons we decided to pursue alternative drug-loading strategies that would not have these limitations. The encapsulation process utilized the evaporation of a solvent (ethanol) to supersaturate and nucleate drug particles by creating a more hydrophobic environment in the interior site of the E2 structure. The maximum ethanol concentration was set at 8% since ethanol is known to be a protein denaturing agent. Previous studies in our lab had confirmed the stability of our scaffold at this percentage through transmission electron microscopy (TEM). Supersaturated solutions of DCF with 8% ethanol were used to nucleate the DCF inside the protein scaffold and co-elution of the protein and the dye was obtained.

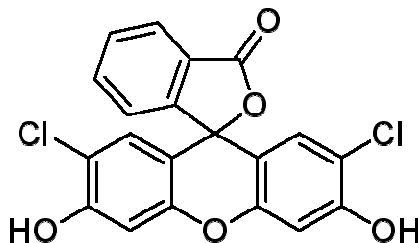


**Figure 3.2** 2',7'-dichlorofluorescein (Sigma)

## 3.2 Materials and Methods

### 3.2.1 Mutagenesis of internal cavity

In order to encapsulate drug molecules inside the nanocapsules, selected amino acids within the cavity were mutated. Mutagenesis of D381F was done by Dr. Sierin Lim and is briefly described here.

Mutagenesis procedure was derived from the Stratagene's QuickChange<sup>®</sup> method (Figure 3.3).

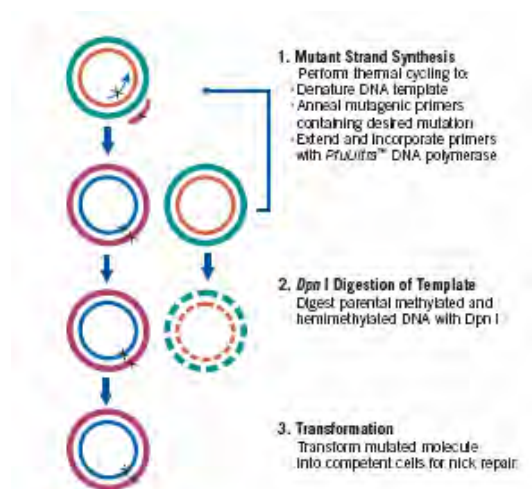


**Figure 3.3** Schematic of the mutagenesis procedure.

First, two complimentary oligonucleotides were designed for codon change at site Asp381 to yield Phe (forward primer showing the mutation site of aspartic acid for phenylalanine in bold: GCC GAA AAG CCG ATC GTT CGT **TTT** GGT GAA ATC GTT GCT GCT CCG). Then, the reaction mixture was prepared as follows: 1  $\mu$ L of template DNA, 1  $\mu$ L Primer mix (20  $\mu$ M), 2  $\mu$ L dNTPs mix (10 mM), 5  $\mu$ L *Pfu* buffer, 1  $\mu$ L *Pfu Ultra* (2.5 U/ $\mu$ L) and 40  $\mu$ L ddH<sub>2</sub>O. The PTC-100 thermal cycler (MJ Research) was programmed with the following cycling parameters: 5 min at 95°C (one cycle); and 30 s

at 95°C, 1 min at 55°C, 1 min/kb of plasmid length at 68°C (18 cycles) and 5 min at 68°C (one cycle) and cool to below 37°C. The amplified PCR fragments were purified using the QIAquick PCR Purification Kit (Qiagen), and then 1 µL of *Dpn* I restriction enzyme (10 U/µL) was added to each reaction mixture and incubated at 37°C for 1 hour to digest the parental supercoiled DNA. Plasmid transformation into *E. coli DH5α* competent cells was performed using a standard heat shock method [47]. Protein expression and purification of mutants were performed.

### **3.2.2 Expression and Purification (1 L batch)**

*E. coli* BL21(DE3) cells transformed with E2-WT and E2-D381F plasmids were grown at 37°C in LB medium supplemented with 100 µg/mL ampicillin. Five-mL from an overnight culture (100 mL) of cells was used to inoculate 1 L of medium. When the OD<sub>600</sub> was between 0.6 and 0.8, the inducer IPTG was added to a final concentration of 1 mM. The cells were harvested 3 h after induction by centrifugation at 6500 *g* for 15 min. *E. coli* cells were resuspended (10 mL/g of wet cells) in 20 mM Tris/HCl, pH 8.7, containing 10 mM EDTA, 0.02% sodium azide, 0.1 mg/mL RNase, 0.1 mg/mL DNase and 1 mM phenylmethylsulfonyl fluoride (PMSF) on ice. The suspension was then disrupted in a French press (Sim Aminco SLM instruments, Inc) under a pressure of 60 MPa. Cell debris was removed by centrifugation at 185000 *g* for 1 h. The supernatant was then heat-treated at 75°C for 20 min to precipitate *E. coli* proteins and centrifuged at 274000 *g* for 1 h. The soluble fraction was applied at a flow rate of 2 mL/min onto a HiPrep 16/10 Q-Sepharose FastFlow anion-exchange column (GE Healthcare), previously equilibrated with 20 mM Tris/HCl, 1 mM EDTA, and 0.02% sodium azide

(pH 8.7). The recombinant protein was eluted in the flow through. Flow through fractions (20 mL) containing the recombinant protein were pooled, concentrated to 1/10 of the volume using a Biomax ultrafiltration disc (Millipore), and loaded (at a flow rate of 1 mL/min) in batches of 5 mL onto a Sepharose 6 prep grade XK 16/70 gel filtration column (GE Healthcare) equilibrated with 20 mM Tris/HCl, 150 mM NaCl, 0.02% sodium azide, and 1 mM EDTA (pH 8.7). Fractions (3.5 mL) containing the pure recombinant protein were pooled. The pooled fractions of recombinant protein were concentrated to approximately 3 mg/mL, frozen and stored at -80°C. The structure of the assembled protein nanoparticles were evaluated by DLS (Malvern Zetasizer Nano-ZS) and TEM (Philips CM-20) and correct protein form was confirmed with MALDI-TOF mass spectrometry (Applied Biosystems Voyager-DE STR). The protein concentration was determined using the Micro BCA Protein Assay kit (Pierce). Total protein yield was 20 mg after purification.

### **3.2.3 DCF standard curves and solubility limits determination**

The primary objective of obtaining standard curves for the model dye (2',7'-dichlorofluorescein, DCF) was to be able to determine the amount of dye in solution through absorbance measurements. Since fluorescein photobleaches, all samples were prepared and kept in the dark.

First, a starting stock solution of 20 mg/mL of DCF in pure ethanol was prepared, and standard solutions were obtained by serial dilutions from the starting stock solution. These standard solutions were added to 20 mM Tris pH 8.7, so that the final percentage of ethanol was 2, 4, 6 and 8%. Note that these standards were vortexed to obtain

homogeneous solutions and spun down at 17500 g for 1 min to eliminate any solid particles in the solution before taking any reading. Following, 200  $\mu$ L of each standard solution was added in a 96-well plate and the absorbance at 503 nm was measured in a microplate reader (Molecular Devices SpectraMax). A full absorbance scan was performed to obtain the wavelength at which absorbance was maximum (503 nm). For the 0% ethanol (buffer only), the starting stock solution was 1.22 mg/mL DCF in 20 mM Tris pH 8.7 and the same procedure was followed.

In order to obtain the solubility limits of DCF at different concentrations of ethanol and different temperatures, two sets of 4 mL solutions of 0, 2, 4, 6 and 8% ethanol in 20 mM Tris pH 8.7 were prepared. A solution of ddH<sub>2</sub>O was used as a control. The experiment was carried out at two different temperatures: room temperature (RT) and 4°C. DCF (0.0025-0.125 g/mL) was added in excess into each solution, so not all of the solid would go into solution. All solutions were stirred for 2 h to obtain a saturated DCF level and allowed to equilibrate for 2 h at the same temperature. After equilibration, samples were syringe-filtered with a 0.2  $\mu$ m porous size filter and appropriate dilutions (using Tris buffer) were done in order to take absorbance readings at the linear range. Repetitions of three were performed to obtain repeatability.

### **3.2.4 Determination of supersaturation required for nucleation**

Since our main aim was to nucleate DCF inside the E2 protein cage, the experimental conditions for this phenomenon to happen were required. Therefore, the goal of these experiments was to determine such experimental conditions at which nucleation of DCF occurs as well as develop an assay to detect it.

Once the solubility limits of the dye were determined at different ethanol concentrations and different temperatures, these values were used as starting points for the present experiment. Two ethanol concentrations were chosen for this study: 4% and 8%. We wanted to be able to reproduce this phase transition at different concentrations of ethanol, and at the same time compare the highest percentage to a lower percentage of ethanol. Since 2% ethanol is a low concentration that was calculated to be not enough for the process of loading the dye inside the capsule, 4% ethanol was picked as the lower value in this experiment. The experiment was performed at RT and 4°C.

First, for each ethanol percentage, three DCF solutions were prepared: one supersaturated, one at saturation and another one below saturation (negative control). In order to start off with all dye in solution (with no precipitation), two solutions of DCF in pure ethanol and in 20 mM Tris pH 8.7 were mixed to the final desired concentrations of dye and ethanol. Six replicates were prepared for each concentration and loaded into a 96-well plate which was stirred for 30 s in the microplate reader.

Second, a turbidity assay was developed to detect precipitation and therefore, nucleation. Absorbance spectra were taken to determine the appropriate wavelengths for turbidity detection. Then, measurements at the selected wavelengths were performed to check for turbidity. The plates were placed in a container saturated with water vapor to ensure just the evaporation of ethanol, not the water. Every 24 h, plates were checked for precipitation using this turbidity assay.

Samples that precipitate formed along time were spun down, and the soluble fraction was taken for measuring the DCF concentration to confirm that it was at expected saturation concentration.

### **3.2.5 Preliminary study on dye-loading experiment**

To prepare protein for dye-loading experiments, the buffer was exchanged into 20 mM Tris/HCl, pH 8.7 and brought to a final concentration of ~5 mg/mL using 2 mL Amicon<sup>®</sup> Centricon<sup>®</sup> centrifugal filter tubes (Millipore). The requirement for such high protein concentration was determined by the small-scale experiment in 96-well microplates. Protein concentration was determined using the Micro BCA Protein Assay kit (Pierce).

The highest percentage of ethanol (8%) was chosen to carry out this set of experiments. Since this is the highest ethanol percentage that we used and the protein was shown to be stable, we decided to first attempt the loading of the capsule with the maximum driving force (degree of supersaturation, which can only be achieved at the highest ethanol percentage).

To obtain the desired DCF concentration, two solutions of DCF were prepared: one in pure ethanol and the other one in 20 mM Tris pH 8.7, and then mixed. The protein in Tris buffer was added to each well so its final concentration was 1 mg/mL. Then they were stirred, loaded into a 96-well microplate, and placed in a container saturated with water vapor for three days to let the ethanol evaporate. Next, samples were checked for precipitation using the turbidity assay and then loaded on a sucrose gradient to determine whether dye and protein were complexed.

### 3.2.6 Sucrose gradient

A discontinuous sucrose density gradient was prepared by layering successive decreasing sucrose density solutions upon one another; therefore the first solution applied is the 50% sucrose solution (see Table 3.1). A steady application of the solutions yields the most reproducible gradient; therefore, the setup described below in Figure 3.4 was followed. First, a thick-wall polycarbonate tube (Beckman) was held upright in a tube stand. Next, a gel loading tip (200  $\mu$ L) was used to load each sucrose solution. Once the 50% solution was loaded, then the following solutions were added by placing the bottom of the tip at the meniscus and gently loading the sucrose solution with a constant flow on top.

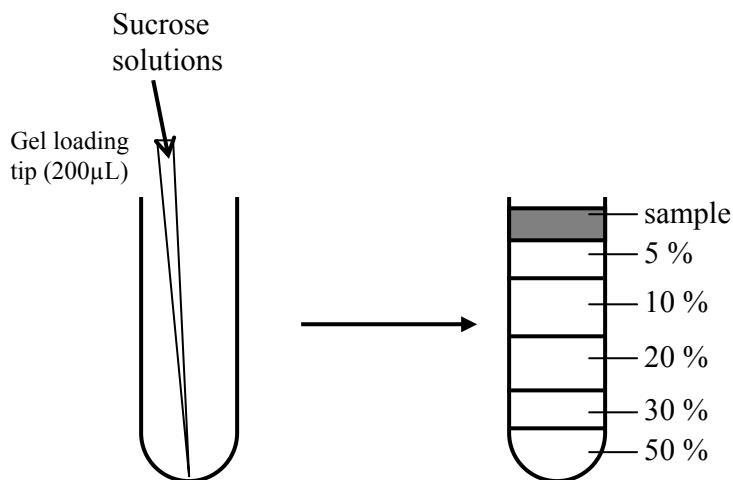


**Figure 3.4** Setup for sucrose gradient preparation

Once the sucrose gradient was formed, discrete layers of sucrose were visible. The sample was applied to the top of the gradient, and the tube was loaded into the TLS-55 rotor (Beckman) very carefully. Ultracentrifugation was started immediately at 111000  $g$  for 2 h at RT with an acceleration profile of 9 and a deceleration profile of 0.

	<b>Solution</b>	<b>Volume (<math>\mu\text{L}</math>)</b>
1 (top)	Sample	200
2	5% sucrose	200
3	10% sucrose	300
4	20% sucrose	300
5	30% sucrose	200
6 (bottom)	50% sucrose	200
		1400 $\mu\text{L}$ total

**Table 3.1** Volumes of solutions used

Immediately after the run, the tubes were removed from the rotor, taking great care not to disturb the sucrose layers. Fractions (100  $\mu\text{L}$ ) were collected from the top using a loading gel tip, by placing the end of the tip right underneath the meniscus.

Collected fractions were then resolved by SDS-PAGE electrophoresis for protein, and the free DCF was determined through absorbance readings at 503 nm.

## **3.3 Results and Discussion**

### **3.3.1 Expression, purification and characterization of proteins**

The E2-WT and mutant D381F were expressed at 37°C and then submitted to the purification process described in section 3.2.2. Both proteins were mostly eluted at 60 mL after injection into the gel filtration column as can be seen in Figure 3.6 for the D381F. It can be observed that there is not a complete separation in the first two peaks. This is confirmed in Figure 3.6, where the D381F was also present in the first peak, although its concentration was considerably lower. The same behavior was observed for E2-WT.

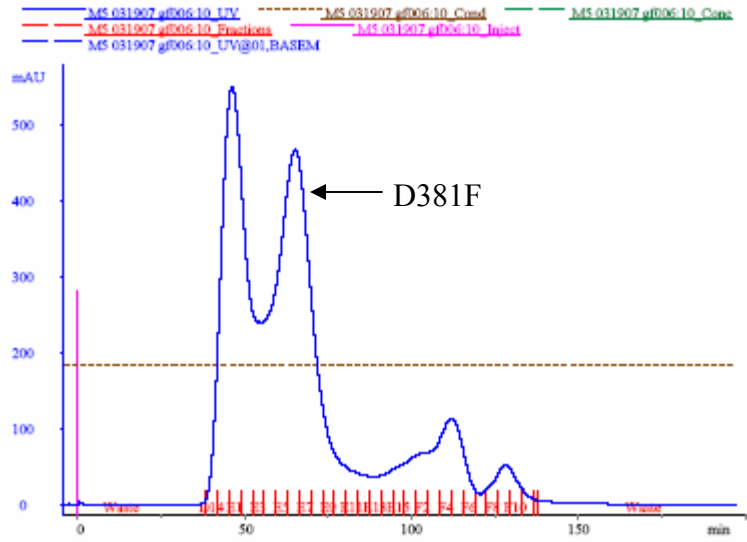


**Figure 3.5** Gel filtration chromatography elution profile of mutant D381F.

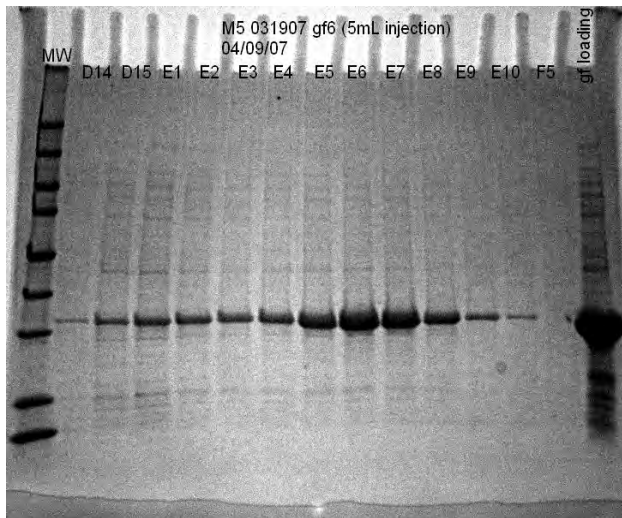


**Figure 3.6** 4-20% Tris-HCl SDS-PAGE of collected fractions after gel filtration chromatography for mutant D381F. Fractions E5 to E8 correspond to second peak in the chromatogram. These fractions were pooled and concentrated for further use.

The SDS-PAGE of the collected fractions during the gel filtration (gf) chromatography (Figure 3.6) shows the higher presence of impurities on the gf loading lane (which corresponds to the fraction injected into the gel filtration column) compared to the fractions collected after this purification step.

Since the concentration of the desired protein in the first peak was low, and to avoid increasing the presence of undesired proteins, only fractions corresponding to the

second peak in the chromatogram were pooled and concentrated to a final concentration of 3 mg/mL. Both proteins (E2-WT and D381F) were then characterized by MALDI-TOF MS and DLS (Figures 3.7 and 3.8). Mass spectrometry confirmed the theoretical molecular weight of a single chain for both E2-WT (experimental mass 28098; calculated mass 28116.6) and D381F (experimental mass 28118.3; calculated mass 28148.7) (see Figure 3.7).

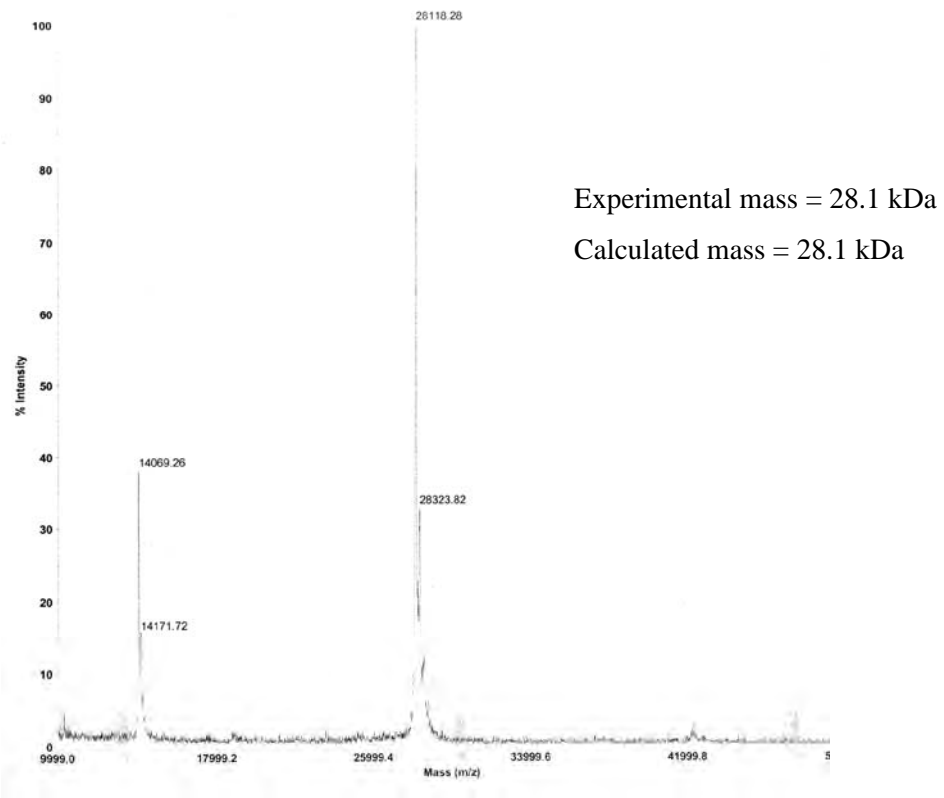


**Figure 3.7** MALDI-TOF MS of mutant D381F confirms single unit (experimental mass 28.1 kDa, calculated mass 28.1 kDa). First peak at 14.1 kDa, corresponds to the double-charged particles.

Table 3.2 shows the hydrodynamic radii of E2-WT and D381F measured by DLS. The measured particle sizes were close to the theoretical size. In our lab, we have observed by means of transmission electron microscopy (TEM) that DLS readings in the range of approximately 25-35 nm still signify a scaffold which self-assembles correctly.

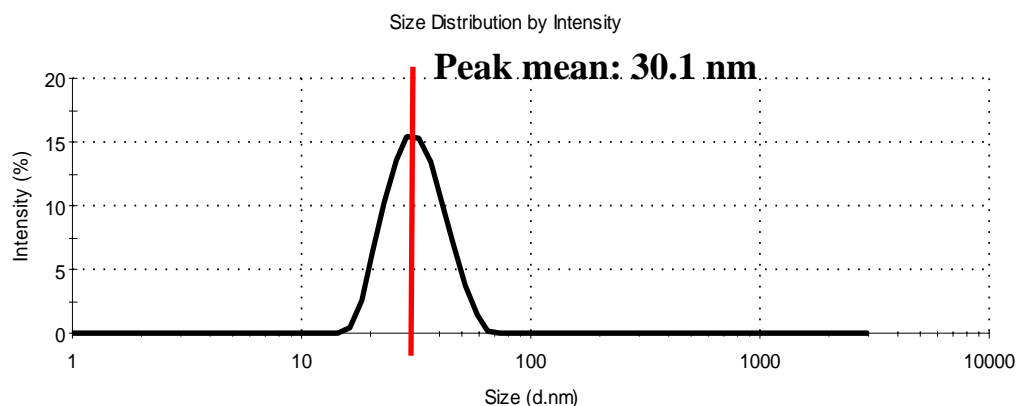


**Figure 3.8** Particle size analysis with DLS confirms overall particle size of the mutant D381F to be approximately 30.1 nm.

Sample	Mean particle size (nm)	# mutations in each cage
WT	30.8	0
D381F mutant	30.1	60

**Table 3.2** Mean particle sizes of E2-WT and mutant M5 measured by DLS. Deviations from the expected 24-nm appear to be related to counterion cloud contribution to particle mobility.

### 3.3.2 DCF standard curves and solubility limits determination

Absorbance spectra of DCF in pure ethanol and 20 mM Tris buffer pH 8.7 were taken (Figure 3.9 and 3.10). DCF showed a maximum absorbance at a wavelength of 503 nm (close to the published 509 nm) and the Tris buffer absorbance was negligible at this wavelength. Therefore, DCF could be diluted in Tris buffer and absorbance measurements taken without any distortion.

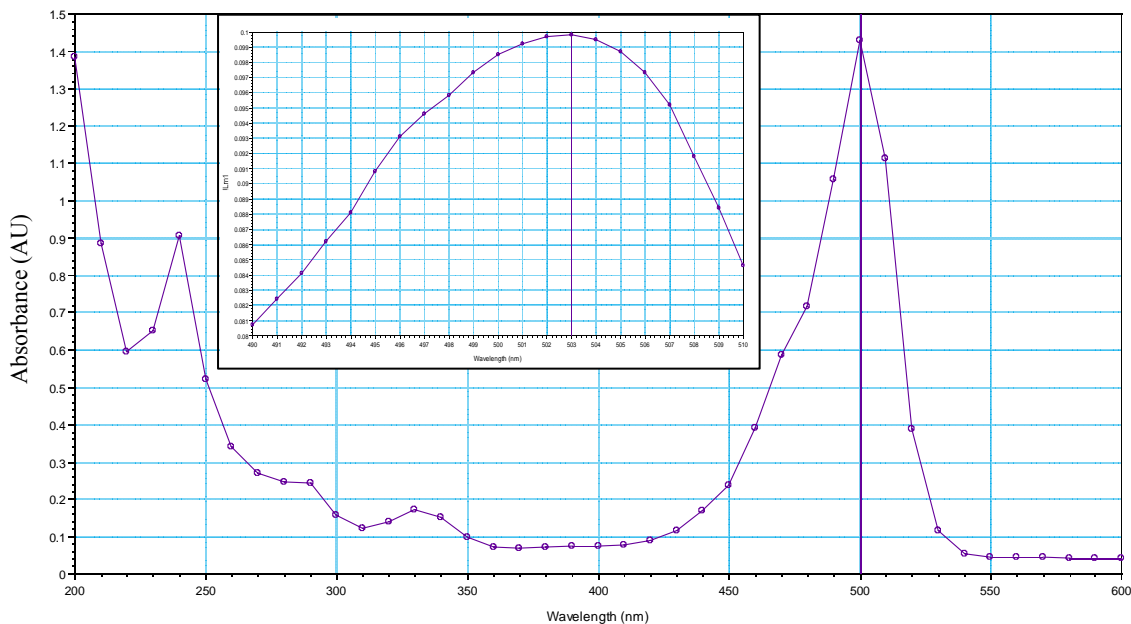


**Figure 3.9** Absorbance spectrum of DCF in pure ethanol ([DCF] = 0.003 mg/mL). Inset spectrum shows the maximum absorbance at 503 nm.

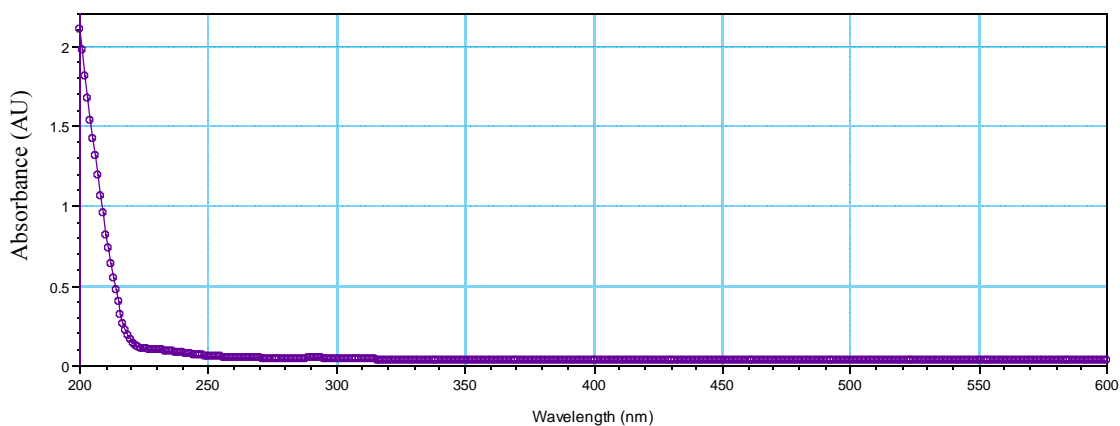


**Figure 3.10** Absorbance spectrum of 20 mM Tris buffer, pH 8.7 showing very low absorbance intensity at 503 nm.

In order to determine the amount of DCF present in solution, a calibration curve was required. Thus, we obtained one for each percentage of ethanol (0, 2, 4, 6, and 8%). Note that since absorbance intensity is pH dependent, pH was carefully checked during all assays.

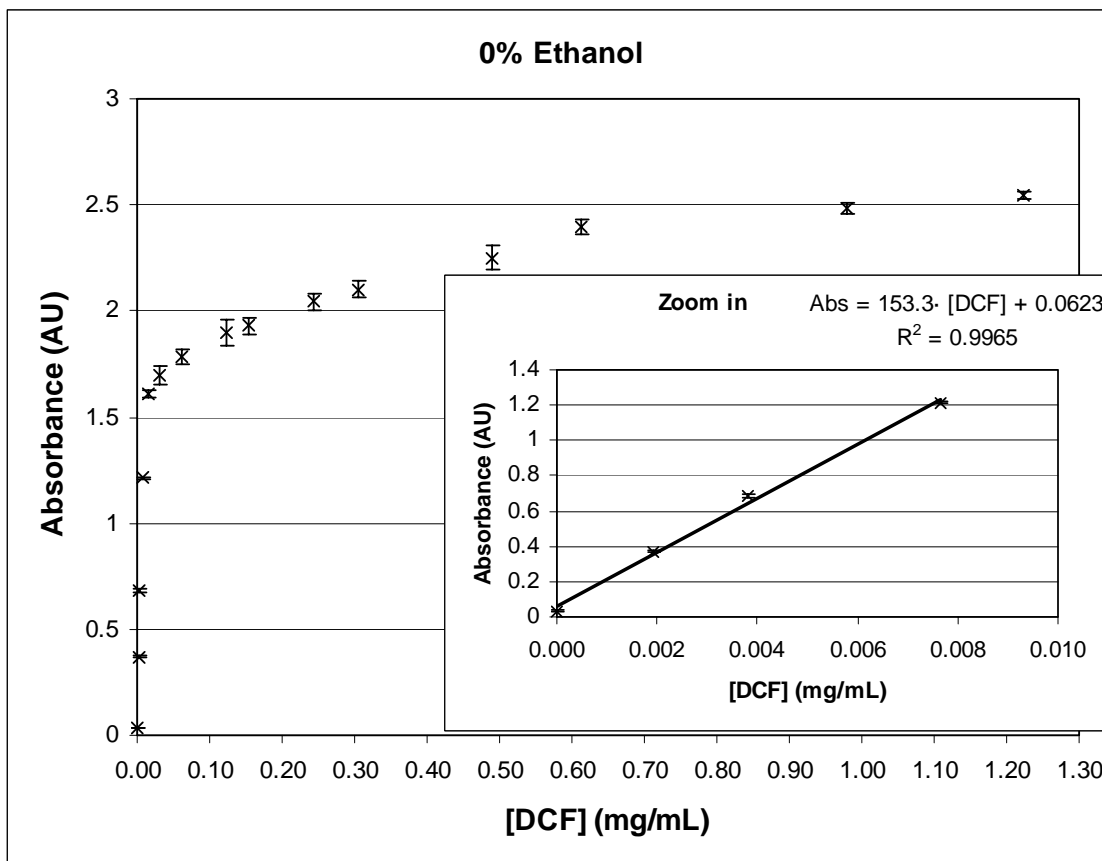


**Figure 3.11** DCF standard curve in 20 mM Tris, pH 8.7. It shows that for the linear range, samples should be diluted below 1.0 AU.

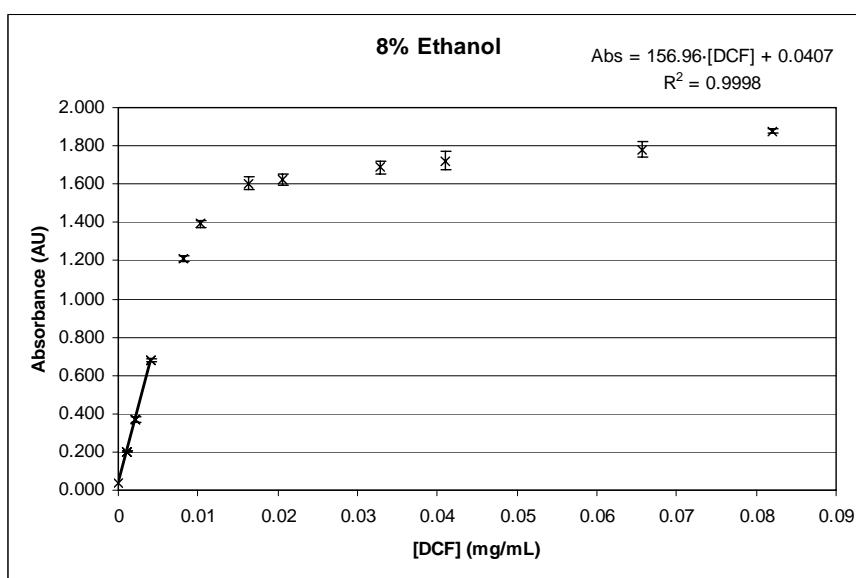


**Figure 3.12** DCF standard curve in 20 mM Tris and 8% ethanol, pH 8.7.

In Figures 3.11 and 3.12, it can be observed that absorbance intensity followed a linear trend with DCF concentration before it saturated. Therefore, we decided to take only those measurements below 1.0 AU and all standard curves were adjusted within that range (see Table 3.3). It was noticed that all standard curves (for any of the tested ethanol percentages) reached absorbance intensity saturation around 1.8 AU, except for the 0% ethanol, which had saturation around 2.5 AU. Moreover, 96-well plates used for this assay were kept at 4°C in the dark for one month, and then readings were taken again to check for any variability. Samples followed the same trend, thus the evaporation effect and any possible degradation of the dye were very low in this time period.

% Ethanol	$y=a\cdot x+b$		
	a	b	R <sup>2</sup>
0	153.3	0.062	0.997
2	173.7	0.050	0.993
4	162.1	0.043	0.998
6	149.8	0.051	0.998
8	156.9	0.041	0.999

**Table 3.3** Coefficients of adjusted linear equations of standard curves at different ethanol percentages.

For the determination of the solubility limits, the supernatants were properly diluted so the absorbance measurements were in the linear range. Figure 3.13A plots the DCF solubility limits performed at room temperature. As can be seen, the solubility increases with the percentage of ethanol which agrees with the higher solubility of DCF in ethanol found in literature (DCF solubility in pure ethanol = 30 mg/mL, in pure water < 0.1 mg/mL). On the other hand, the experiment carried out at 4°C (Figure 3.13B) showed no clear trend. No reason could be found to explain this behavior.

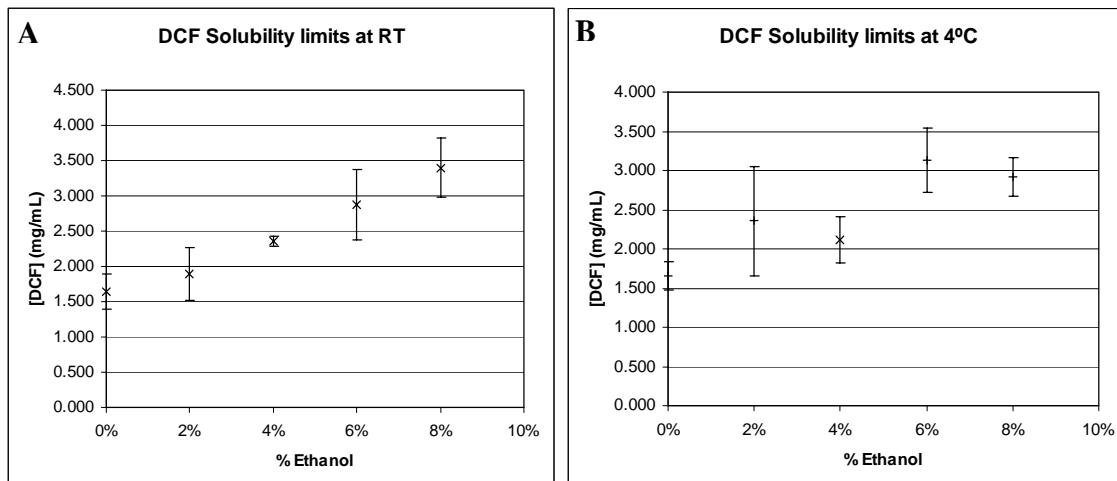


**Figure 3.13** DCF solubility limits in Tris buffer at A) room temperature and B) 4°C. At RT DCF solubility increases with the percentage of ethanol, but at 4°C it does not follow a clear trend.

Note in Figure 3.13 that at 0% ethanol (only Tris buffer) the DCF solubility is higher than the published solubility in water (< 1 mg/mL) which we confirmed in our water controls. This effect is due to the Tris buffer which also helps solubilize the dye.

### 3.3.3 Determination of supersaturation conditions

Since DCF solubility limits at 4°C showed no clear trend, we decided to follow with the supersaturation experiments just at room temperature.

For determining the optimal wavelength for measuring turbidity, all samples were submitted for a full absorbance spectra reading.

**Figure 3.14** shows that at wavelengths above 600 nm the absorbance is low relative to the maximum dye absorbance. Therefore, 600 and 650 nm were chosen as the best wavelengths for turbidity measurements since the absorbance of the dye is low and it could be experimentally checked that these wavelengths give higher absorbance intensity

when precipitation occurs than at 700 nm or higher. Thus, the solution-to-solid phase transition of the dye molecule can be detected.

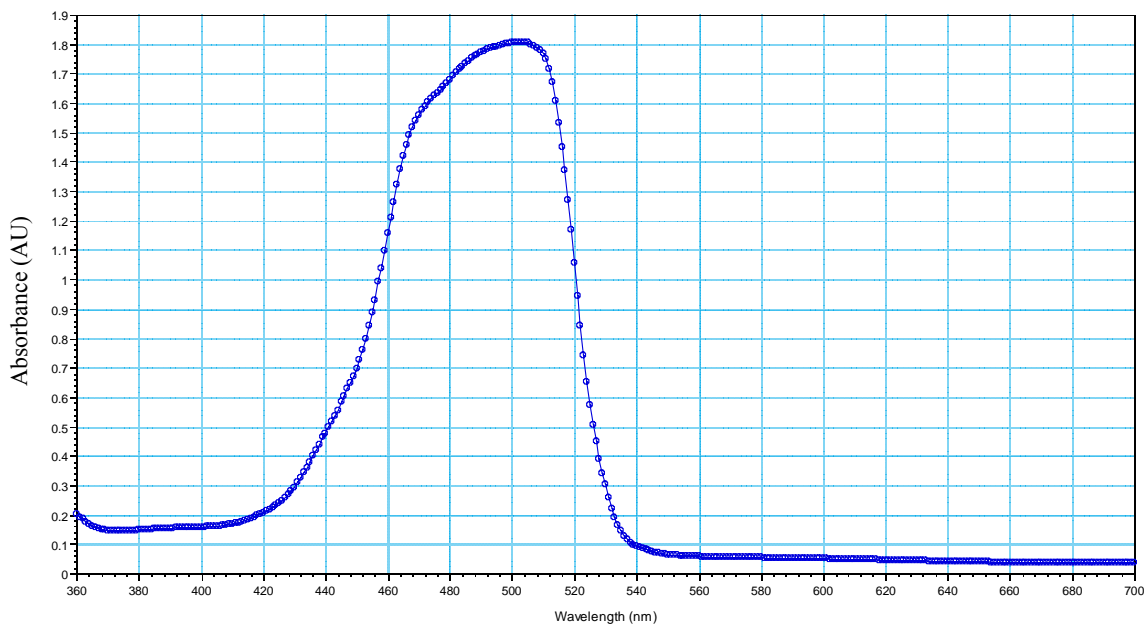


**Figure 3.14** Absorbance spectra of DCF solution (0.034 mg/mL) in 20 mM Tris and 8% ethanol pH 8.7 shows that turbidity can be measured at 650 or 700 nm with a very low interference of the dye signal.

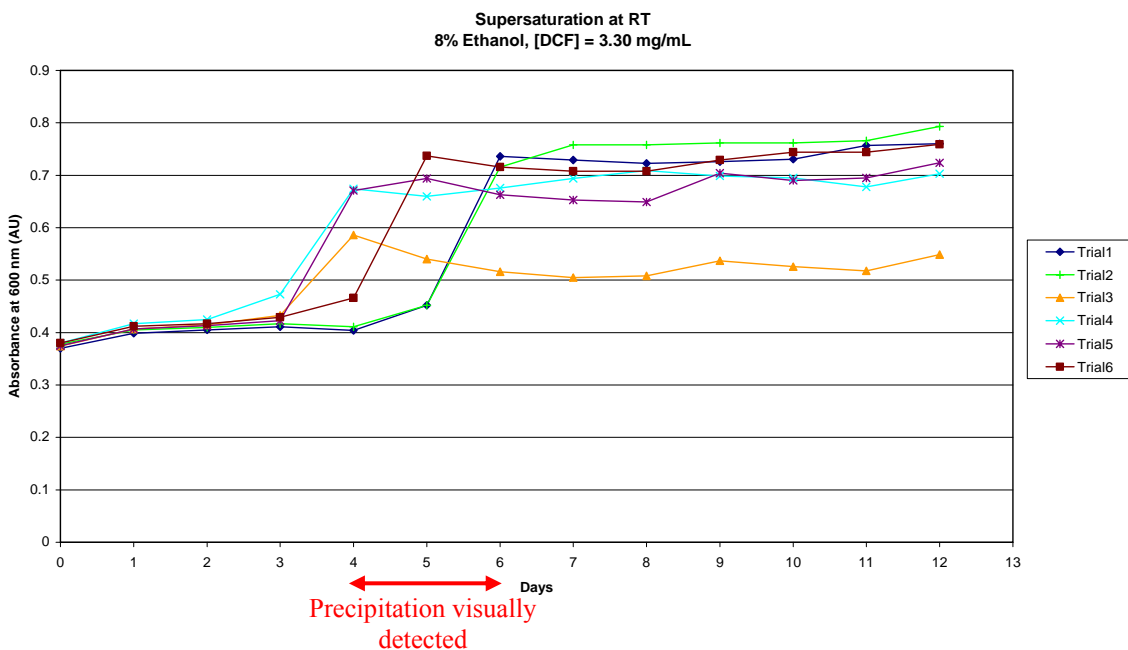


**Figure 3.15** Six replicates of supersaturation phenomenon at 8% ethanol and room temperature ([DCF]=3.3 mg/mL). Samples started precipitating between days 4 to 6, and stochastic nature of nucleation was observed. Absorbance readings were taken at 600 nm.

Figure 3.15 shows the results of one set of turbidity assays to determine dye precipitation. The absorbance at 600 nm versus time is plotted for an 8% ethanol saturated solution ( $[DCF] = 3.30 \text{ mg/mL}$ ). As ethanol completely evaporated, samples became supersaturated and precipitated between days 4 to 6 and the stochastic nature of nucleation was observed. For the samples ( $[DCF] = 3.79 \text{ mg/mL}$ ) that are initially supersaturated, precipitation was detected after 24 h (data not shown). For those samples below saturation concentration ( $[DCF] = 3.13 \text{ mg/mL}$ ), absorbance remained constant during 13 days and no precipitate was visible (data not shown).

Solutions at 4% ethanol showed a different behavior. Samples below saturation ( $[DCF] = 1.21 \text{ mg/mL}$ ) were kept in solution for 13 days and absorbance remained constant, as expected. For samples at saturation ( $[DCF] = 2.30 \text{ mg/mL}$ ) and at supersaturation ( $[DCF] = 2.65 \text{ mg/mL}$ ), however, no nucleation was observed. Hence, it was decided to add a supplemental amount of DCF dissolved in pure ethanol after day 6 so the concentration of DCF would be near saturation at 8% ethanol ( $3.44 \text{ mg/mL}$ ). Five to six days after the supplementary addition of DCF, precipitation was detected. This shows that precipitation and nucleation is not always attainable, even at supersaturation conditions.

The supernatant of two samples from the supersaturation experiment at 8% ethanol were checked at 503 nm for DCF concentration. DCF level was calculated to be around  $3.79 \text{ mg/mL}$ , considerably higher than expected. Thus, it appears that not all the ethanol was evaporated.

### 3.3.4 Preliminary results on dye-loading experiment and sucrose gradient

In our preliminary data on loading experiments with DCF, we found that the sequence for mixing the solutions was important. In the first attempt, the protein was first mixed with the DCF in Tris buffer. When the DCF in pure ethanol was added, precipitation was observed, together with the formation of aggregates on the surface of the liquid. For the best results (and to keep the mixture in solution), the protein had to be the last addition. The reason why the first procedure did not work is uncertain, but ethanol may induce some change in the media or dye when added, and this causes the protein to precipitate.

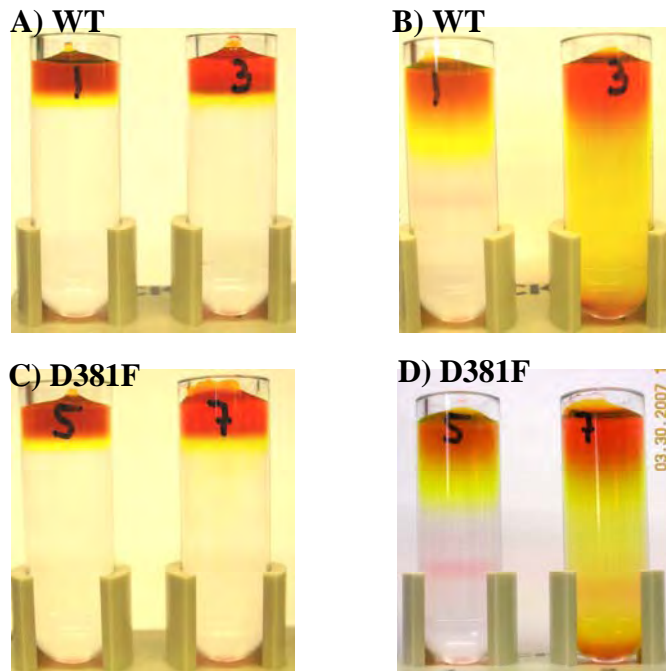


**Figure 3.16** Sucrose gradients: A) E2-WT before centrifuging, B) E2-WT after centrifuging, C) D381F before centrifuging, D) D318F after centrifuging. Tubes # 1 and 5 were loaded with [DCF]=1.5 mg/mL; and 3 and 7, with [DCF]=3.3 mg/mL.

Figure 3.16 shows one of the two sets of sucrose gradients for E2-WT and mutant D381F before and after centrifugation. It can be seen that for tubes number 1 and 5, which were loaded with a DCF concentration below saturation ( $[DCF]=1.5$  mg/mL), the dye remains in the top fractions after centrifugation. In tubes 3 and 7, which were loaded with  $[DCF]=3.3$  mg/mL (at saturation prior to ethanol evaporation), however, the dye was present all along the gradient and some pellet was collected in the bottom of the tubes. Experiments were performed in duplicate and results were similar.

In the following chart (Figure 3.17) the DCF concentration was calculated for each of the collected fractions from the absorbance measurements at 503 nm and the average of two trials is plotted. This concentration was determined as if all the ethanol was evaporated. The plot shows that as a result of the diffusion mechanism of the dye through the gradient, the majority of the dye was collected in the top six fractions. Notice also that for the solutions at an initial DCF saturation concentration, the amount of DCF increased about 0.4 mg/mL in the bottom fraction. Two possible explanations could be given to this observation. The dye either undergoes nucleation and precipitation outside the protein scaffolds or nucleation takes place inside the protein core. In order to know which phenomenon is occurring further investigation will be conducted.

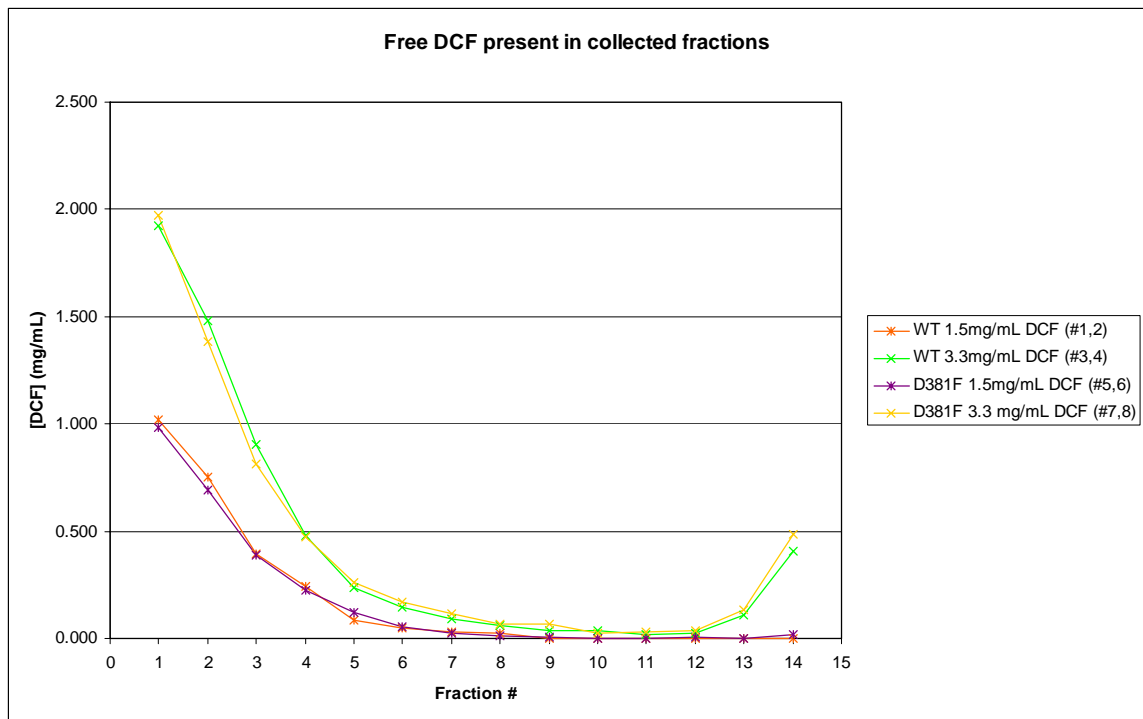


**Figure 3.17** Free DCF present in collected fractions (the average of two repeats is shown for each condition). All gradients loaded with a solution at the DCF saturation concentration showed a precipitate in the bottom of the gradient tubes which was confirmed with absorbance measurements at 503 nm.

The technique used to collect the fractions of the gradients after centrifugation was shown to be adequate for these experiments even though some residual dye is always dragged into the bottom fractions. As can be seen in Figure 3.17, for those gradients where the DCF could be separated in the top fractions, the remaining amount of dye is minimal. Furthermore, this method allows the precise acquisition of small volumes that could not be done by collecting fractions from the bottom of the tube after puncturing it.

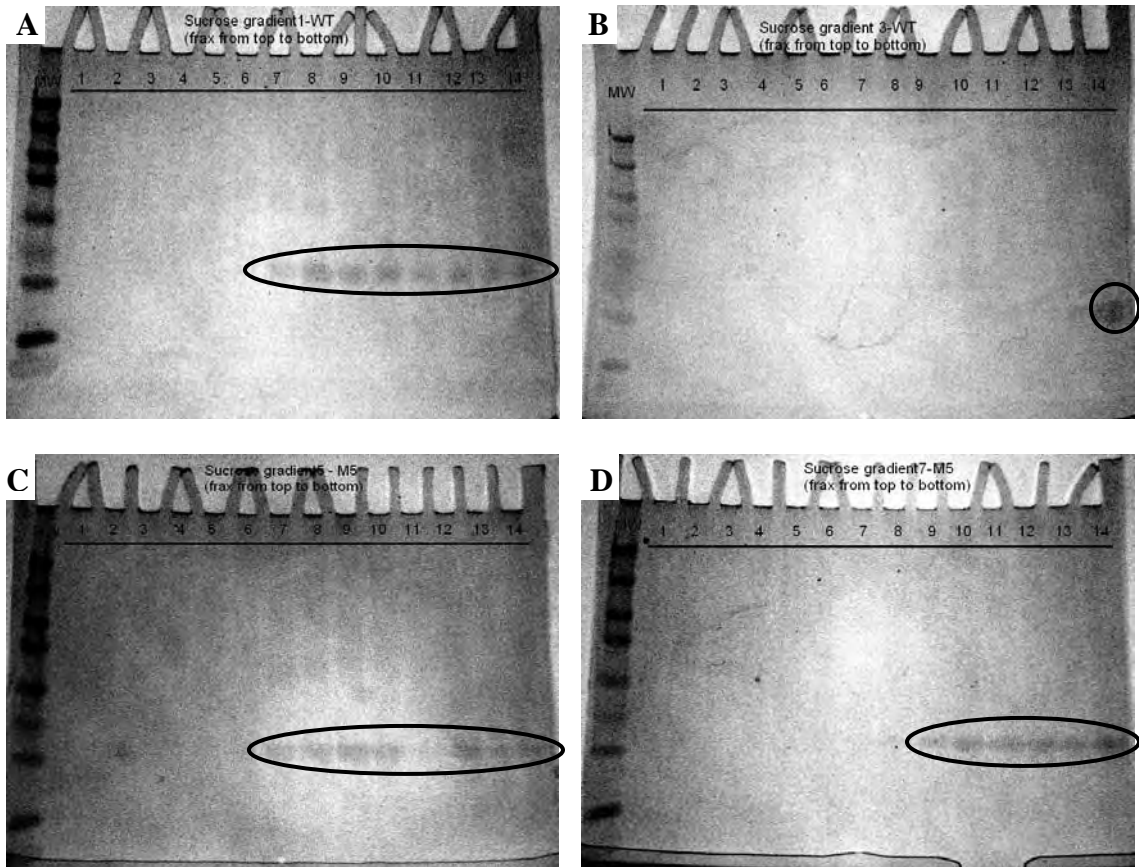


**Figure 3.18** 4-20% Tris-HCl SDS-PAGE of collected fractions for each of the sucrose gradients. Fraction numbering starts from 1, top to 14, bottom. Gels A and B correspond to the WT with 1.5 mg/mL DCF and 3.3 mg/mL DCF, respectively. Gels C and D correspond to the D381F with same DCF concentration.

Figure 3.18 shows the SDS-PAGE of each gradient for both WT and D381F for the same experiment shown in Figure 3.16. Except for the E2-WT with a DCF concentration below saturation (1.5 mg/mL) and the mutant D381F at the same DCF concentration, the rest of the gradients showed that the protein co-eluted with the dye. These duplicated results show the co-elution of dye and protein in the lower fractions. So as ethanol evaporates, dye is less soluble, and then it precipitates at hydrophobic nucleation points. But further investigation needs to be done in order to detect whether the nanocapsules were loaded or not. The gradient also should be optimized in order to separate loaded capsules from non-loaded.

# Chapter 4

## Conclusions

The E2 component of the pyruvate dehydrogenase multienzyme complex from *Bacillus stearothermophilus* is a protein scaffold in the nanometer scale of great potential utility. This domain can generate a pentagonal dodecahedral scaffold with icosahedral symmetry, composed of 60 E2 monomers. In this work, we showed the ability to express and characterize different functional peptides on the outer surface of the nanocage. In particular, we reproduced Domingo's work and expressed the malaria epitope (MAL1) [30], and three peptides for tumor targeting (cyclic RGD-4C, RGD linear and LTV). Only the cyclic RGD-4C was expressed with comparable levels as the MAL1; therefore it was further purified and characterized by dynamic light scattering (DLS) and SDS-PAGE gel. Another peptide for nucleation of quantum dots was studied, but expression was detected in small yields in the insoluble fractions and further investigation needs to be performed with the soluble fractions.

Another functionality of this scaffold is the potential ability to encapsulate drug molecules inside the hollow core. Here we presented our preliminary results on

hydrophobic dye nucleation inside the nanocage. We were able to genetically modify the interior surface of the scaffold while keeping its self-assembling capacity and the nucleation phenomenon was attempted twice after establishing all the required experimental conditions (working percentage of ethanol, supersaturation concentration of dye and temperature). Our preliminary data showed promise since both dye and protein co-eluted in a sucrose gradient separation, although further work is required to detect loaded nanocapsules.

This work also helped to establish methodic protocols for protein purification, sucrose gradient, and turbidity determination that will be of great utility in future steps of this project.

# Chapter 5

## Future work

Future work will involve further studies on the expression of the quantum dot peptide (J140) as well as those peptides expressed in lower amounts (RGD linear and LTV) compared to the controls (E2-WT and E2-MAL1). After the synthesis and characterization of these fusion proteins, we will examine their ability to target cancer cells. We will use human breast carcinoma cells which have been reported to contain a receptor that binds to the RGD peptide sequence. Also, we will investigate the nature for the insolubility of the expressed quantum dot (J140) and study the potential ability of the scaffold as an imaging agent. Ultimately, we will engineer the scaffold to display multiple functional peptides on the outer surface and evaluate their performance.

As for the hydrophobic dye-loading approach, we have developed a fluorescence assay to quickly detect both protein and dye prior to running SDS-PAGE gels on sucrose gradient fractions. The sucrose gradient needs to be optimized for separation of loaded and non-loaded capsules and characterization of loaded capsules needs to be performed.

Further studies will involve encapsulation of drugs covalently linked to fluorescent probes that will allow quantification of the amount of drug released inside cells.

# References

1. Lipinski, C.A., *Poor Aqueous Solubility - an Industry Wide Problem in Drug Discovery*. American Pharmaceutical Review, 2002. **5**(3): p. 82-85.
2. Radtke, M., *Pure drug nanoparticles for the formulation of poorly soluble drugs*. New Drugs, 2001(3): p. 62-68.
3. Christie, R.J. and D.W. Grainger, *Design strategies to improve soluble macromolecular delivery constructs*. Advanced Drug Delivery Reviews Biomedical Micro- and Nano-technology, 2003. **55**(3): p. 421-437.
4. Rosler, A., G.W.M. Vandermeulen, and H.-A. Klok, *Advanced drug delivery devices via self-assembly of amphiphilic block copolymers*. Advanced Drug Delivery Reviews Polymeric Materials for Advanced Drug Delivery, 2001. **53**(1): p. 95-108.
5. Vinogradov, S.V., T.K. Bronich, and A.V. Kabanov, *Nanosized cationic hydrogels for drug delivery: preparation, properties and interactions with cells*. Advanced Drug Delivery Reviews, 2002. **54**(1): p. 135-147.
6. Svenson, S. and D.A. Tomalia, *Dendrimers in biomedical applications--reflections on the field*. Advanced Drug Delivery Reviews Dendrimers: a Versatile Targeting Platform, 2005. **57**(15): p. 2106-2129.

7. Qiu, L. and Y. Bae, *Polymer Architecture and Drug Delivery*. Pharmaceutical Research, 2006. **23**(1): p. 1-30.
8. Ogawara, K.-I., et al., *Uptake by hepatocytes and biliary excretion of intravenously administered polystyrene microspheres in rats*. Journal of Drug Targeting, 1999. **7**(3): p. 213-221.
9. Douglas, T. and M. Young, *Host-guest encapsulation of materials by assembled virus protein cages*. 1998. **393**(6681): p. 152-155.
10. Helene Braun, K.B., Johannes L&ouml;wer, Wolf Martin Bertling, Andreas Zimmer, *Oligonucleotide and plasmid DNA packaging into polyoma VP1 virus-like particles expressed in Escherichia coli*. Biotechnology and Applied Biochemistry, 1999. **29**(1): p. 31-43.
11. Beames, B. and R. Lanford, *Insertions within the hepatitis B virus capsid protein influence capsid formation and RNA encapsidation*. J. Virol., 1995. **69**(11): p. 6833-6838.
12. Schmidt, U., R. Rudolph, and G. Bohm, *Binding of external ligands onto an engineered virus capsid*. Protein Eng., 2001. **14**(10): p. 769-774.
13. Peabody, D., *A Viral Platform for Chemical Modification and Multivalent Display*. Journal of Nanobiotechnology, 2003. **1**(1): p. 5.
14. Wang, Q., et al., *Natural Supramolecular Building Blocks: Cysteine-Added Mutants of Cowpea Mosaic Virus*. Chemistry & Biology, 2002. **9**(7): p. 813-819.
15. Kathryn M. Taylor, T.L., Claudine Porta, Anne G. Mosser, Heidi A. Giesing, George P. Lomonosoff, John E. Johnson,, *Influence of three-dimensional*

- structure on the immunogenicity of a peptide expressed on the surface of a plant virus.* Journal of Molecular Recognition, 2000. **13**(2): p. 71-82.
16. Flenniken, M.L., et al., *The Small Heat Shock Protein Cage from Methanococcus jannaschii Is a Versatile Nanoscale Platform for Genetic and Chemical Modification.* Nano Lett., 2003. **3**(11): p. 1573-1576.
  17. Flenniken, M.L., et al., *Melanoma and Lymphocyte Cell-Specific Targeting Incorporated into a Heat Shock Protein Cage Architecture.* Chemistry & Biology, 2006. **13**(2): p. 161-170.
  18. Meldrum, F.C., et al., *Synthesis of inorganic nanophase materials in supramolecular protein cages.* 1991. **349**(6311): p. 684-687.
  19. Manchester, M. and P. Singh, *Virus-based nanoparticles (VNPs): Platform technologies for diagnostic imaging.* Advanced Drug Delivery Reviews Particulate Nanomedicines, 2006. **58**(14): p. 1505-1522.
  20. Brannon-Peppas, L. and J.O. Blanchette, *Nanoparticle and targeted systems for cancer therapy.* Advanced Drug Delivery Reviews Intelligent Therapeutics: Biomimetic Systems and Nanotechnology in Drug Delivery, 2004. **56**(11): p. 1649-1659.
  21. Dixit, S.K., et al., *Quantum Dot Encapsulation in Viral Capsids.* Nano Lett., 2006. **6**(9): p. 1993-1999.
  22. Uchida, M., et al., *Targeting of Cancer Cells with Ferrimagnetic Ferritin Cage Nanoparticles.* J. Am. Chem. Soc., 2006. **128**(51): p. 16626-16633.
  23. Douglas, T. and M. Young, *Viruses: Making Friends with Old Foes.* Science, 2006. **312**(5775): p. 873-875.

24. Flenniken, M.L., et al., *Selective attachment and release of a chemotherapeutic agent from the interior of a protein cage architecture*. Chemical Communications, 2005(4): p. 447-449.
25. Gupta, S.S., et al., *Accelerated Bioorthogonal Conjugation: A Practical Method for the Ligation of Diverse Functional Molecules to a Polyvalent Virus Scaffold*. Bioconjugate Chem., 2005. **16**(6): p. 1572-1579.
26. Raja, K.S., et al., *Hybrid Virus-Polymer Materials. 1. Synthesis and Properties of PEG-Decorated Cowpea Mosaic Virus*. Biomacromolecules, 2003. **4**(3): p. 472-476.
27. Milne, J.L.S., et al., *Molecular architecture and mechanism of an icosahedral pyruvate dehydrogenase complex: a multifunctional catalytic machine*. The EMBO Journal, 2002. **21**(21): p. 5587-5598.
28. Milne, J.L.S., et al., *Molecular Structure of a 9-MDa Icosahedral Pyruvate Dehydrogenase Subcomplex Containing the E2 and E3 Enzymes Using Cryoelectron Microscopy*. J. Biol. Chem., 2006. **281**(7): p. 4364-4370.
29. Izard, T., et al., *Principles of quasi-equivalence and Euclidean geometry govern the assembly of cubic and dodecahedral cores of pyruvate dehydrogenase complexes*. PNAS, 1999. **96**(4): p. 1240-1245.
30. Domingo, G.J., S. Orru', and R.N. Perham, *Multiple Display of Peptides and Proteins on a Macromolecular Scaffold Derived from a Multienzyme Complex*. Journal of Molecular Biology, 2001. **305**(2): p. 259-267.
31. Ruoslahti, E. and M. Pierschbacher, *New perspectives in cell adhesion: RGD and integrins*. Science, 1987. **238**(4826): p. 491-497.

32. Koivunen, E., B. Wang, and E. Ruoslahti, *Phage Libraries Displaying Cyclic Peptides with Different Ring Sizes: Ligand Specificities of the RGD-Directed Integrins*. 1995. **13**(3): p. 265-270.
33. Arap, W., R. Pasqualini, and E. Ruoslahti, *Cancer Treatment by Targeted Drug Delivery to Tumor Vasculature in a Mouse Model*. *Science*, 1998. **279**(5349): p. 377-380.
34. Assa-Munt, N., et al., *Solution Structures and Integrin Binding Activities of an RGD Peptide with Two Isomers*. *Biochemistry*, 2001. **40**(8): p. 2373-2378.
35. Balasubramanian, S. and D. Kuppuswamy, *RGD-containing Peptides Activate S6K1 through  $\beta$ 3 Integrin in Adult Cardiac Muscle Cells*. *J. Biol. Chem.*, 2003. **278**(43): p. 42214-42224.
36. Zitzmann, S., V. Ehemann, and M. Schwab, *Arginine-Glycine-Aspartic Acid (RGD)-Peptide Binds to Both Tumor and Tumor-Endothelial Cells in Vivo*. *Cancer Res*, 2002. **62**(18): p. 5139-5143.
37. KIM, J.-W. and H.-S. LEE, *Tumor targeting by doxorubicin-RGD-4C peptide conjugate in an orthotopic mouse hepatoma model*. *International Journal of Molecular Medicine*, 2004. **14**(4): p. 529-535.
38. SHADIDI, M. and M. SIOUD, *Identification of novel carrier peptides for the specific delivery of therapeutics into cancer cells*. *FASEB J.*, 2003. **17**(2): p. 256-258.
39. Bruchez, M., Jr., et al., *Semiconductor Nanocrystals as Fluorescent Biological Labels*. *Science*, 1998. **281**(5385): p. 2013-2016.

40. Colvin, V.L., M.C. Schlamp, and A.P. Alivisatos, *Light-emitting diodes made from cadmium selenide nanocrystals and a semiconducting polymer*. 1994. **370**(6488): p. 354-357.
41. Mao, C., et al., *Viral assembly of oriented quantum dot nanowires*. PNAS, 2003. **100**(12): p. 6946-6951.
42. Flynn, C.E., et al., *Synthesis and organization of nanoscale II-VI semiconductor materials using evolved peptide specificity and viral capsid assembly*. Journal of Materials Chemistry, 2003. **13**(10): p. 2414-2421.
43. Mulder, W.J.M., et al., *Quantum Dots with a Paramagnetic Coating as a Bimodal Molecular Imaging Probe*. Nano Lett., 2006. **6**(1): p. 1-6.
44. Lessard, I.A.D., et al., *Expression of genes encoding the E2 and E3 components of the Bacillus stearothermophilus pyruvate dehydrogenase complex and the stoichiometry of subunit interaction in assembly in vitro*. European Journal of Biochemistry, 1998. **258**(2): p. 491-501.
45. Allen, M.D. and R.N. Perham, *The catalytic domain of dihydrolipoyl acetyltransferase from the pyruvate dehydrogenase multienzyme complex of Bacillus stearothermophilus: Expression, purification and reversible denaturation*. FEBS Letters, 1997. **413**(2): p. 339-343.
46. Domingo, G.J., et al., *Induction of specific T-helper and cytolytic responses to epitopes displayed on a virus-like protein scaffold derived from the pyruvate dehydrogenase multienzyme complex*. Vaccine, 2003. **21**(13-14): p. 1502-1509.

47. Sambrook, J. and G.J. Russel, *Molecular cloning: A laboratory manual*. 3rd edition 2001 ed. 2001, Cold Spring Harbor: New York: Cold Spring Harbor Laboratory Press.
48. Lathrop, R.H., et al., *Method for producing a synthetic gene or other DNA sequence*. 2005: US.
49. Fernández-Nieves, A., A. Fernández-Barbero, and F.J. de las Nieves, *Particle-counterion clustering in highly charge-asymmetric complex fluids*. *Physical Review E: Statistical, Nonlinear, and Soft Matter Physics*, 2001. **63**(4): p. 041404/1-041404/5.
50. Lewis, J.D., et al., *Viral nanoparticles as tools for intravital vascular imaging*. 2006. **12**(3): p. 354-360.
51. SCHMIDT, U., et al., *Protein and peptide delivery via engineered polyomavirus-like particles*. *FASEB J.*, 2001. **15**(9): p. 1646-1648.
52. Douglas, T. and M. Young, *Host-guest encapsulation of materials by assembled virus protein cages*. *Nature*, 1998. **393**(6681): p. 152-155.
53. Eatock, M., et al., *Activity of Doxorubicin Covalently Bound to a Novel Human Serum Albumin Microcapsule*. *Investigational New Drugs*, 1999. **17**(2): p. 111-120.
54. Weber, C., et al., *Desolvation process and surface characterisation of protein nanoparticles*. *International Journal of Pharmaceutics*, 2000. **194**(1): p. 91-102.
55. Kreuter, J., et al., *Covalent attachment of apolipoprotein A-I and apolipoprotein B-100 to albumin nanoparticles enables drug transport into the brain*. *Journal of Controlled Release*, 2007. **118**(1): p. 54-58.

56. Stehle G, et al., *Albumin-based drug carriers: comparison between serum albumins of different species on pharmacokinetics and tumor uptake of the conjugate*. *Anticancer Drugs*, 1999. **10**(8): p. 785-790.
57. Urry, D.W., *Entropic elastic processes in protein mechanisms. I. Elastic structure due to an inverse temperature transition and elasticity due to internal chain dynamics*. *Journal of Protein Chemistry*, 1988. **7**(1): p. 1-34.
58. Herrero-Vanrell, R., et al., *Self-assembled particles of an elastin-like polymer as vehicles for controlled drug release*. *Journal of Controlled Release*, 2005. **102**(1): p. 113-122.
59. Seelig, A., *A general pattern for substrate recognition by P-glycoprotein*. *European Journal of Biochemistry*, 1998. **251**(1-2): p. 252-261.
60. Gottesman, M.M., *MECHANISMS OF CANCER DRUG RESISTANCE*. *Annual Review of Medicine*, 2002. **53**(1): p. 615-627.
61. Zgurskaya, H.I. and H. Nikaido, *Multidrug resistance mechanisms: drug efflux across two membranes*. *Molecular Microbiology*, 2000. **37**(2): p. 219-225.
62. Yu, E.W., et al., *Structural Basis of Multiple Drug-Binding Capacity of the AcrB Multidrug Efflux Pump*. *Science*, 2003. **300**(5621): p. 976-980.
63. Loo, T. and D. Clarke, *Functional consequences of phenylalanine mutations in the predicted transmembrane domain of P-glycoprotein*. *J. Biol. Chem.*, 1993. **268**(27): p. 19965-19972.
64. Loo, T.W., M.C. Bartlett, and D.M. Clarke, *Transmembrane segment 7 of human P-glycoprotein forms part of the drug-binding pocket*. *Biochemical Journal*, 2006. **399**(2): p. 351-359.